Mémoire

Auteur : Martin, Aurore
Promoteur(s) : Absil, Olivier; Orban De Xivry, Gilles
Faculté : Faculté des Sciences
Diplôme : Master en sciences spatiales, à finalité approfondie
Année académique : 2024-2025
URI/URL : http://hdl.handle.net/2268.2/22971

Observing solar system objects with METIS

Master thesis carried out in partial fulfillment of the requirements for the Master's degree in Spaces Sciences, research focus

Author: Aurore Martin

Academic supervisors: Olivier Absil, Gilles Orban de Xivry

Jury members: Emmanuel Jehin, Bertrand Bonfond

University of Liège

Faculty of Sciences

Academic year 2024-2025

ABSTRACT

Observations with the Mid-infrared ELT Imager and Spectrograph (METIS) at the upcoming Extremely Large Telescope (ELT) are expected to significantly enhance mid-infrared astronomy, offering new insights into topics such as protoplanetary disks, galaxy physics, and solar system objects. Due to the ELT large aperture, the METIS instrument will include an adaptive optics (AO) system. This AO system relies only on natural guide stars, which imposes stringent constraints on the observability of fast-moving solar system targets.

This thesis presents a study of the observation possibilities of solar-system objects with METIS, taking into account the constraints from its AO system. This work covers various aspects, from the development of a tool aiming at identifying suitable observation windows for solar system objects to the study of different targets.

The constraints affecting observability—guide star brightness, angular separation, target motion, and observing conditions like Sun and target elevation—are first identified and implemented in the algorithm. The tool is then applied to various target types, revealing that fast-moving objects like Mercury, or comets close to their perihelion do not allow a guide star to remain close enough for a sufficiently long time to enable a proper observations. Similarly, Mars and main-belt asteroids offer only short windows, while slower targets like outer planets or trans-Neptunian objects allow longer observations, though low stellar density can still be a limiting factor, especially for the slowest objects.

The impact of a more restrictive field of view and star brightness is also studied, showing that the most restrictive case of stars brighter than magnitude 12 often ensures an average of 10 windows per year, though it may require to put the target off-axis in the science camera, which would result in reduced operation capabilities.

The study finally explores the potential of using asteroids and trans-Neptunian objects themselves as guide stars, expanding observing possibilities for otherwise challenging targets.

Keywords: astronomy, extremely large telescope, adaptive optics, solar system objects

ACKNOWLEDGMENTS

First of all, I would like to thank my supervisors, Olivier Absil and Gilles Orban de Xivry, for the time they took to review my work as well as for proposing this thesis topic, which allowed me to combine the knowledge I acquired during my five years of engineering studies with what I discovered this year while studying space sciences. Their guidance and insightful reviews over the past few weeks have helped clarifying and strengthening the content of this study.

I would also like to thank the two other members of my jury, Emmanuel Jehin and Bertrand Bonfond, for the valuable information they provided throughout the year for the various test cases, as well as for the time they dedicated to evaluating this thesis.

I must also thank my family who supported me during this work but also throughout my studies. In particular I want to thank my parents for the taste of curiosity they instilled in me. I would not be here without you.

Finally, I want to thank all the friend I have made during my six years at university, as well as those who have been part of my life even longer. Thank you for all the board game nights, the balls, and all the laughter that made these years truly memorable.

CONTENTS

Acronyms **ix**

Scope of and goals of the work **1**

1 Adaptive optics **2**
1.1 General principles 2
1.2 From wavefront sensing to correction 4
1.3 Guide stars 5
1.4 The different types of adaptive optics 6

2 The METIS instrument **7**
2.1 The Extremely Large Telescope 7
2.2 The METIS instrumental layout 8
2.3 Performance of the METIS adaptive optics system 11

3 Reference systems and reference frames **13**
3.1 Difference between reference system and reference frame 13
3.2 International Celestial Reference System and Frame 14
3.3 Geocentric Celestial Reference System and Frame 15
3.4 Jupiter System III 16

4 Searching for off-axis guide stars **17**
4.1 Requirements 17
4.2 Observability assessment tool principles 19
4.2.1 Search for stars around the target 20
4.2.2 Search for sufficiently long windows 23
4.2.3 Representations of observation windows 25
4.2.4 Time step 26

5 Results of the search **29**
5.1 Planets 29

5.2 Main-belt asteroids . . . 33
5.3 Trans-Neptunian objects . . . 35
5.4 Comets . . . 37
5.5 Moons . . . 41
5.6 Jupiter's aurorae . . . 43
5.7 Discussion . . . 46
5.7.1 Influence of guide star magnitude . . . 46
5.7.2 Influence of angular separation between target and guide star . . . 47
5.7.3 Influence of target configuration . . . 47

6 On-axis guiding on science targets 49
6.1 Constraints . . . 49
6.2 Asteroids . . . 50
6.2.1 Asteroid magnitude . . . 50
6.2.2 Results . . . 52
6.3 Trans-Neptunian objects . . . 57

Conclusion and perspectives 58

Bibliography 62

LIST OF FIGURES

1.1 Bright star observed without adaptive optics with a long exposure (left) or a short one (center) and corrected for atmospheric turbulence (right) . . . 2
1.2 General concept of adaptive optics system . . . 3

2.1 Optical design of the ELT . . . 8
2.2 Conceptual set-up of METIS . . . 9
2.3 METIS fields of view. . . . 10
2.4 METIS AO system performance in terms of Strehl ratio as a function guide star K magnitude. . . . 11
2.5 Degradation of the Strehl ratio as a function of the distance to the guide star for a median seeing and $z = 30^\circ$ . . . 12

3.1 Right ascension and declination as seen from outside the celestial sphere . 14
3.2 Relationship between the ICRS coordinates returned by `JPL Horizons` and those considered in the `ICRS` class of `Astropy`. . . . 15
3.3 Representation of Jupiter System III . . . 16

4.1 Illustration of on-axis and off-axis guiding on a solar system target. . . . 18
4.2 Main principles of the tool developed to asses the observability of a solar system object. . . . 19
4.3 Block diagram of the search for times when there are stars around the science target. . . . 21
4.4 Representation of the three possible configurations of the search region around the target. . . . 22
4.5 Block diagram of the search for sufficiently long windows. . . . 24
4.6 Example of representation of observation windows - Uranus observation window of November 25, 2032 - $m_{\mathrm{K,\,min}} = 12$ - $\Delta t = 10$ min - `Astropy` ephemerides. . . . 26
4.7 Hygiea observation window of July 23, 2034 - $m_K < 12$ - $\Delta t = 5$ min - JPL ephemerides. . . . 27

4.8 Mars observation window of January 23, 2031 - $m_K < 14$ - $\Delta t = 5$ min - JPL ephemerides. 28

5.1 Scatter plot of observation window duration as a function of guide star magnitude for windows in which at least a part of the limb of Mars is observable - $\Delta t = 1$ min - `Astropy` ephemerides. 31
5.2 Mars observation window of February 3, 2033 - $m_K < 12$ - $\Delta t = 1$ min - `Astropy` ephemerides. 31
5.3 Scatter plot of observation window duration as a function of guide star magnitude for windows in which at least a part of the limb of Uranus is observable - $\Delta t = 10$ min - `Astropy` ephemerides. 32
5.4 Differences between Uranus observation windows of December 4, 2034 obtained with `Astropy` or `JPL Horizons` ephemerides - $\Delta t = 10$ min. 33
5.5 Uranus observation window of November 30, 2031 - $m_K < 12$ - $\Delta t = 10$ min - `JPL Horizons` ephemerides. 34
5.6 Scatter plot of observation window duration as a function of guide star magnitude for windows in which at least a part of the limb of Hygiea is observable - $\Delta t = 5$ min - `JPL Horizons` ephemerides. 35
5.7 Scatter plot of observation window duration as a function of guide star magnitude for windows in which at least a part of the limb of Vesta is observable - $\Delta t = 5$ min - `JPL Horizons` ephemerides. 35
5.8 Scatter plot of observation window duration as a function of guide star magnitude for windows in which at least a part of the limb of Pluto is observable - $\Delta t = 10$ min - `JPL Horizons` ephemerides. 36
5.9 Scatter plot of observation window duration as a function of guide star magnitude for windows in which at least a part of the limb of 67P is observable - $\Delta t = 5$ min - `JPL Horizons` ephemerides. 38
5.10 Observations windows of 67P when the comet is closer than 2 AU from the Sun - $m_K < 14$ - $\Delta t = 1$ min - `JPL Horizons` ephemerides. 39
5.11 Scatter plot of observation window duration as a function of guide star magnitude for windows in which at least a part of the limb of C/2024 E1 is observable with a minimum elevation of 0° - $\Delta t = 5$ min - `JPL Horizons` ephemerides. 40
5.12 Scatter plot of observation window duration as a function of guide star magnitude for windows in which at least a part of the limb of C/2014 UN271 is observable - $\Delta t = 10$ min - `JPL Horizons` ephemerides. 40
5.13 Observation window of C/2014 UN271 on January 22, 2031 - $m_K < 12$ - $\Delta t = 10$ min - `JPL Horizons` ephemerides. 41
5.14 Scatter plot of observation window duration as a function of guide star magnitude for windows in which at least a part of the limb of Io is observable - $\Delta t = 10$ min - `JPL Horizons` ephemerides. 42
5.15 Io observation windows - $d_{\text{Io - Jupiter}} = 13.5$" - $m_K < 12$ - $\Delta t = 10$ min - `JPL Horizons` ephemerides. 43

5.16 Projected views of Jupiter's north and south polar regions. Grid lines indicate System III longitude and planetocentric latitude lines 43
5.17 Jupiter aurorae observation windows - $m_K < 12$ - $\Delta t = 10$ min - `JPL Horizons` ephemerides. 44
5.18 Scatter plot of observation window duration as a function of guide star magnitude for observations of a part of Jupiter's auroral ovals - $\Delta t = 10$ min - `JPL Horizons` ephemerides. 45
5.19 Jupiter aurorae observation windows only enabling to observe a small fraction of the aurora - $m_K < 12$ - $\Delta t = 10$ min - `JPL Horizons` ephemerides. . 46

6.1 Variation of asteroid apparent magnitude as a function of their diameter for different albedos - $d_{\mathrm{AS}} = 2.10$ AU - $V - K = 2.5$ mag. 53
6.2 Variation of asteroid apparent magnitude as a function of their diameter for different albedos - $d_{\mathrm{AS}} = 2.65$ AU - $V - K = 2.5$ mag. 53
6.3 Variation of asteroid apparent magnitude as a function of their diameter for different albedos - $d_{\mathrm{AS}} = 3.20$ AU - $V - K = 2.5$ mag. 54
6.4 Variation of asteroid apparent magnitude as a function of their diameter for different albedos - $d_{\mathrm{AS}} = 5.20$ AU - $V - K = 2.5$ mag. 54
6.5 Size distribution of asteroids, with the cumulative number larger than a given diameter plotted against diameter (km). 56

LIST OF TABLES

5.1 Number of observation windows of at least 30 min for Uranus in different configurations - $\Delta t = 10$ min - `Astropy` and `JPL Horizons` ephemerides. . 32
5.2 Number of observation windows of at least 30 min for Hygiea and Vesta in different configurations - $\Delta t = 5$ min - `JPL Horizons` ephemerides. 34
5.3 Number of observation windows of at least 30 min for Pluto in different configurations - $\Delta t = 10$ min - `JPL Horizons` ephemerides. 36
5.4 Number of observation windows of at least 30 min for the three comets - $\Delta t = 5$ min for C/2024 E1 and 67P and $\Delta t = 10$ min for C/2014 UN271 - `JPL Horizons` ephemerides. 37
5.5 Number and maximum duration of observation windows of 67P for different maximum heliocentric distances - $m_K < 14$ - $\Delta t = 5$ min - `JPL Horizons` ephemerides. 38
5.6 Number of observation windows of at least 30 min for Io in different configurations - $\Delta t = 10$ min - `Astropy` and `JPL Horizons` ephemerides. . . . 41
5.7 Number of observation windows of at least 30 min for Jupiter's aurorae in different configurations - $\Delta t = 10$ min - `JPL Horizons` ephemerides. 44

6.1 Average G_1 and G_2 parameters for main asteroid classes. 51
6.2 Average geometric albedos for main asteroid classes. 51
6.3 Minimum and maximum diameter enabling main-belt asteroids to be used in the AO system with $m_K < 14$ for various asteroid-Sun distance and minimum and maximum phase angles. 55
6.4 Same as Table 6.3 in the case of Jupiter trojans which consist mostly of D-type asteroids. 55

ACRONYMS

2MASS Two Micron All Sky Survey

ANDES ArmazoNes high Dispersion Echelle Spectrograph

AO adaptive optics

CFO Common Fore Optics

ELT Extremely Large Telescope

ESO European Southern Observatory

FoV field of view

FWHM Full width at half maximum

GCRF Geocentric Celestial Reference Frame

GCRS Geocentric Celestial Reference System

HARMONI High Angular Resolution Monolithic Optical and Near-infrared Integral field spectrograph

ICRF International Celestial Reference Frame

ICRS International Celestial Reference System

LGS laser guide star

METIS Mid-infrared ELT Imager and Spectrograph

MICADO Multi-AO Imaging Camera for Deep Observations

MORFEO Multiconjugate adaptive Optics Relay For ELT Observations

MOSAIC Multi-Object Spectrograph

NGS natural guide star

SCAO single-conjugate adaptive optics

TNO trans-Neptunian object

XAO extreme adaptive optics

SCOPE OF AND GOALS OF THE WORK

Among the various intruments of the upcoming Extremely Large Telescope (ELT), the Mid-infrared ELT Imager and Spectrograph (METIS) will enable significant progress in observations performed in the mid-infrared range. These advances are expected to bring a new light on subjects as diverse as protoplanetary disk and the formation of planets, detection and characterization of exoplanets, the formation history of the Solar System, massive stars and cluster formation, evolved stars and their circumstellar environment, the galactic center, physics of galaxies and active galactic nuclei [1].

To perform such observations, the METIS instrument will be equipped with an adaptive optics (AO) system. Although adaptive optics on the ELT can in principle be performed using laser or natural guide stars, on METIS, only natural guide stars will be used. For observations of objects without proper motion, determining observability is thus straightforward: either the object itself can serve as guide star, or a sufficiently bright star is present within the field of view. If neither condition is met, the object cannot be observed with METIS. In contrast, scheduling solar system object observations will be more challenging. Indeed since solar system objects display a large proper motion, the availability of a suitable guide star within the field of view will depend on the specific time of observation. It is thus necessary to determine the times for which a suitable guide star lies close enough to the science target and then to asses if the star remains for a sufficiently long time in the field of view to ensure a proper observation window.

This thesis therefore focuses on the development of a tool to determine the observation windows and their duration for solar system objects such as planets, asteroids or comets with the help of the `Astropy` [2, 3] and the `JPL Horizons` system [4]. To do so, a general introduction to adaptive optics is first given. The METIS instrument is then described along with its expected performance and limitations. A brief presentation of the different reference systems and reference frames used during the development of the tool is then presented before presenting the main algorithms developed for this thesis. These algorithms are then applied to a selection of targets representing the variety of objects within the solar system. Finally, the possibility of using solar system objects such as asteroids or trans-Neptunian objects (TNOs) as guide object for the adaptive optics system is assessed.

CHAPTER 1

ADAPTIVE OPTICS

This chapter aims to review the fundamental principles of adaptive optics, as described in [5, 6, 7, 8]. The main objective behind adaptive optics systems is first reminded before discussing several key aspects of such systems such as wavefront sensing, reconstruction and correction. Afterwards, the two types of guide stars are described and the different types of adaptive optics systems reviewed.

1.1 General principles

When the light from an astronomical object goes through the atmosphere, atmospheric turbulence causes the light from an object to spread out as illustrated in Figure 1.1 for a long exposure and a short one. This blurring effect is caused by the temperature fluctuations in small patches of air leading to different refractive indices between the patches. Since light rays are refracted many times, this creates differential delays and small changes in the direction of propagation. The wavefront is therefore distorted and, when the rays reach the telescope, they are no longer parallel and thus can not be focused into a single point anymore, leading to a blurred image.

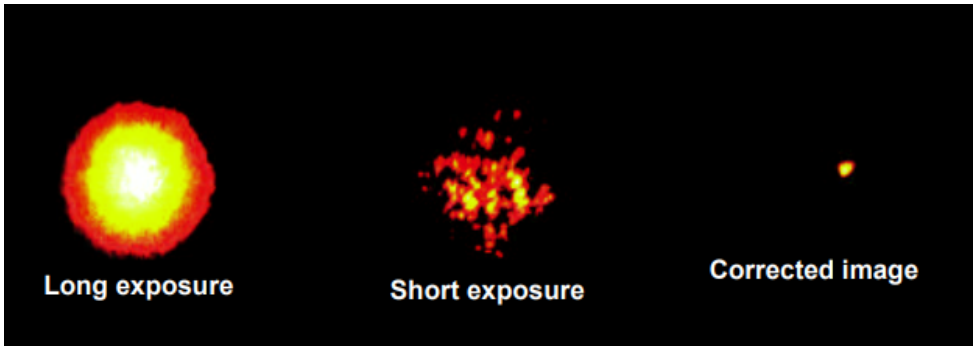

Figure 1.1: Bright star observed without adaptive optics with a long exposure (left) or a short one (center) and corrected for atmospheric turbulence (right) (Credits: Center for Adaptive Optics, UC Santa Cruz).

The turbulence strength can be characterized by the Fried parameter, r_0, which is defined as the diameter of a circular area over which the RMS wavefront aberration due to atmospheric turbulence is equal to 1 radian [9]. This can be seen as a coherence length and has a value around 15-20 cm at $\lambda = 500$ nm for good observing sites. If the diameter D of a telescope is larger than r_0, the point-spread-function, *i.e.*, the image of a point source, is no longer diffraction-limited. The Full width at half maximum (FWHM) of a long exposure image is proportional to λ/r_0 which can be way larger than the theoretical 1.22 λ/D of a diffraction-limited system. Any telescope with such diameter therefore has no better spatial resolution than a telescope of diameter r_0. This limitation is particularly problematic for telescopes such as the ELT where the ratio D/r_0 is so high that it becomes essential to correct this effect in order to recover the telescope full angular resolution.

Adaptive optics systems are used to counteract this effect and enable diffraction-limited observations. To do so, a dichroic beamsplitter separates a fraction of the target light from the main science beam, based on wavelength. This light is then sent to a wavefront sensor that measures several hundreds to a few thousands of time per second how the incoming wavefront is distorted by atmospheric turbulence. This information is then used by a computer to determine how to adjust the shape of the deformable mirror of the telescope in order to cancel out the distortions due to turbulence. As illustrated in Figure 1.2, this process forms a closed-loop system so that the deformable mirror shape is continuously modified in order to adjust its shape to the small errors present downstream of the deformable mirror. As atmospheric turbulence changes over a timescale of a few milliseconds, the higher the AO loop frequency, the more accurate the correction.

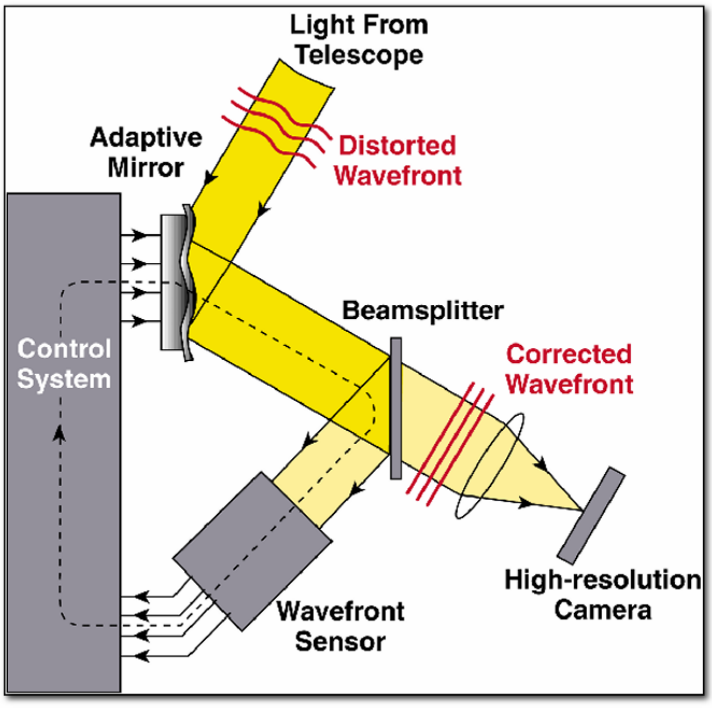

Figure 1.2: General concept of adaptive optics system (Credits: Center for Adaptive Optics, UC Santa Cruz).

If the science target is too faint or too extended, its light cannot be used to reliably measure the wavefront distortions. In such cases, another star within the field of view (FoV) can be used as a guide star. However, since this star is offset from the science target, its light does not travel through exactly the same path in the atmosphere. Thus, the distortion caused by atmospheric turbulence is slightly different and, as a consequence, since the correction applied to the mirror is based on the guide star, it is not optimal for the science target. This phenomenon is known as anisoplanatism. Consequently, the larger the angular separation between the guide star and the science target, the less effective the adaptive optics corrections will be for the target.

The efficacy of the correction provided by an adaptive optics system can be measured through the Strehl ratio, *i.e.*, the ratio between the peak intensity of the corrected point spread function and the peak intensity in the perfect diffraction-limited case. Therefore, the higher the Strehl ratio, the better the image correction.

1.2 From wavefront sensing to correction

Since optical and infrared detectors cannot directly measure phase aberrations with the sensitivity required for astronomical applications, wavefront sensors instead encode phase variations into measurable intensity variations.

The most simple wavefront sensor is the Shack-Hartmann wavefront sensor where the incoming wavefront is divided into sub-apertures by an array of microlenses. Each microlens then focuses the light onto a detector where it forms a spot. If the part of the wavefront going through the microlens is flat, the spot appears at its expected position on the detector. On the other hand, if the local wavefront is tilted, the spot is shifted proportionally. Measuring this shift therefore enables to determine the local slope of the wavefront and by combining all the local measurements the global wavefront can be reconstructed.

On modern AO systems, the Shack-Hartmann wavefront sensor is usually replaced by a pyramid wavefront sensor that uses a pyramidal prism in the focal plane to produce four images of the pupil. In order to determine the wavefront slope, the position of the beam has to be modulated so that a ray passes some time in each of the four quadrants, the ratio of the time spent in each quadrant depending on the ray position with respect to the pyramid vertex. The modulation frequency is equal to an integer multiple of the integration time of the detector, ensuring that the beam spends an equal amount of time in each quadrant so that the resulting signal is properly averaged. Moreover, the modulation radius determines the sensitivity and the dynamic range. A small radius leads to more sensitivity whereas a larger radius enables to obtain a larger dynamic range. The main advantage of this type of wavefront sensor is that its resolution is set by the diffraction limit of the telescope. Moreover, in closed-loop mode, the signal-to-noise ratio obtained with a pyramid wavefront sensor is better than with a Shack-Hartmann wavefront sensor, especially for low order aberrations. This enables a gain of about 2 magnitudes in sensitivity on natural guide stars and is thus more and more used.

There also exists a few other wavefront sensor concepts such as the lateral shearing interferometer or the curvature wavefront sensor but none of them is used anymore in modern AO systems.

The detectors used in the wavefront sensors need to have a rapid readout, a low noise so that faint guide stars can be used, and a large number of pixels in order to have a good wavefront sampling. In most cases, electron-multiplying CCD or CMOS sensors are used for sensing in the visible whereas avalanche photo-diodes are preferred in for near infra-red measurements.

The measurements performed with the wavefront sensor are then used to reconstruct the full wavefront in order to compute the appropriate correction on the deformable mirror. This reconstruction process relies on an interaction matrix that relates the sensor measurements to the actuator commands. These commands are then applied in order to locally modify the surface of the deformable mirror so that it corrects the incoming wavefront. For modern telescopes such as the ELT, the most common type of deformable mirrors are the thin facesheet mirrors with actuators on their backside.

1.3 Guide stars

Regarding the guide star used to measure the wavefront, it can either be a natural star or a laser star.

Natural guide stars (NGSs) are, as their name indicates, real stars whose light travels through (almost) the same part of the atmosphere as the science target. In order to provide enough light to the wavefront sensor so that the wavefront distortion is properly measured, such stars much be bright enough, typically brighter than magnitude 14 in the V-band [8]. The science target is generally used as guide star but if it is too faint or too extended, another star can be used as guide star provided it is sufficiently bright. This star must however be sufficiently close to the science target to ensure that their light goes through similar atmospheric turbulence. Indeed, if the separation between the guide star and the target is too large, anisoplanatism effects become too important and the quality of the correction is severely degraded. Since the maximum separation is typically smaller than 20", the probability to find a suitable star is, on average, lower than 1 %, though it would be larger in the galactic plane and lower at the galactic poles. This thus puts a stringent constraint on the observation possibilities.

On the other hand, laser guide stars (LGSs) enable to observe a larger part of sky by projecting a laser beam into the atmosphere. The most common laser guide stars are the sodium LGSs. With such a guide star, the laser excites sodium atoms in the mesosphere, *i.e.*, around 90 km of altitude. Spontaneous decay of these excited atoms then produces a resonant backscatter. The laser wavelength must therefore be specifically tuned to corresponds to the desired atomic transitions and can either be pulsed or continuous. Six of these lasers will be installed on the ELT.

This type of guide stars is however associated to some drawbacks. First, it is more complex and expensive to implement than NGSs and it requires specific hardware in

terms of wavefront sensor. Secondly, the sodium layer in the mesosphere can vary in time which can lead to variation of the flux received by the AO system. The fluctuation of the vertical distribution of sodium can also lead to focus errors in the adaptive optics systems. Moreover, laser guide stars also come with some spot elongation because of the thickness of the sodium layer. Besides, whereas the light of a natural guide star samples a cylindrical volume because it comes from an infinite distance, the light from a laser guide star only passes through a conical volume. There is thus some turbulence affecting the science target that is not measured with the LGS and this focus anisoplanatism decreases the AO performance. Finally, LGSs do not enable to measure the tip-tilt of the image. Indeed because the laser guide star is created at a finite altitude in the atmosphere, the upward and downward paths of the laser beam both introduce positional shifts that do not correspond exactly to the true tip-tilt motion of the incoming wavefront from the science target. To counteract this effect, a natural star must be used to measure and correct the tip-tilt. Thanks to the correction provided by the LGS and the fact that only tip-tilt needs to be measured, this star can however be much fainter than those used for NGSs, therefore enabling to observe more parts of the sky.

1.4 The different types of adaptive optics

The most simple type of AO is the single-conjugate adaptive optics (SCAO) which uses only one guide star that is generally a natural star. This type of AO system is however limited in terms of field of view because of anisoplanatism, *i.e.*, the fact that the wavefront distortion is not the same in two different lines of sight. This causes an elongation of the spots towards the guide star. Additionally, for laser guide stars, the cone effect mentioned in section 1.3 also has a strong impact on image quality.

To mitigate this effect, tomographic techniques have been implemented in order to reconstruct the turbulence inside the full cylinder of air above the telescope mirror, using measurements from several guide stars spread across the field of view. By combining the information from different lines of sight, it then becomes possible to estimate how turbulence is distributed at different altitudes or in different pointing directions. For example, several lasers can be used to correct the cone effect and to optimize on-axis correction. Using several deformable mirrors, each of them coupled to an atmospheric layer or to a target depending on the technique, with several natural or laser guide stars can also enable to overcome the size limitation of the field of view due to anisoplanatism and increase its size.

Besides tomography, another type of AO systems are the extreme adaptive optics (XAO) systems. Such systems enable to obtain the best correction currently possible but on a very narrow field of view, typically of the order of a few arcseconds. This method operates at high temporal frequencies in order to follow rapid atmospheric changes and requires a high actuator density on the deformable mirror so that fine-scale turbulence can be corrected.

CHAPTER 2

THE METIS INSTRUMENT

In this chapter, several key aspects of the METIS instrument are described. First, a brief summary about the Extremely Large Telescope and its instruments is given. Then, the instrumental layout of METIS is described along with the performance of its adaptive optics system along with the resulting limitations in terms of observations.

2.1 The Extremely Large Telescope

The ELT is a next-generation ground based observatory currently constructed by the European Southern Observatory (ESO) at the top of Cerro Amazones in Chile [10, 11, 12]. The ELT's most prominent feature is its 38 m segmented concave primary mirror, which consists of 798 hexagonal segments. This large collecting area will enable the telescope to gather more light than any previous optical or infrared telescope, improving its ability to detect faint and distant objects. This will also enable to achieve a resolving power approximately four times greater than the one of current 8–10 meter class telescopes, allowing it to resolve objects that are up to four times closer on the sky. As shown in Figure 2.1, this mirror sends the light to the convex 4.25 m secondary mirror and then to the 4 m third mirror. After that, the light reaches the fourth mirror. This mirror is a facesheet mirror and will perform the corrections related to atmospheric turbulence before sending it to the fifth mirror that will correct for the tip-tilt errors and send the light to one of the two Nasmyth platforms. This design will provide a 10 arcmin unvignetted FoV and the fourth and fifth mirrors will enable to reach the telescope diffraction limit by correcting for atmospheric turbulence and vibrations of the telescope structure.

The ELT will be equipped with several instruments, six of them being already planned. Two instruments will start operations at or near the telescope first light that is currently planned around 2030: METIS, that will enable imaging and spectroscopy in the mid-infrared, and the Multi-AO Imaging Camera for Deep Observations (MICADO) that will take high-resolution images in the near-infrared. The diffraction-limited resolution of MICADO wide-field images will be made possible thanks to the Multiconjugate adaptive

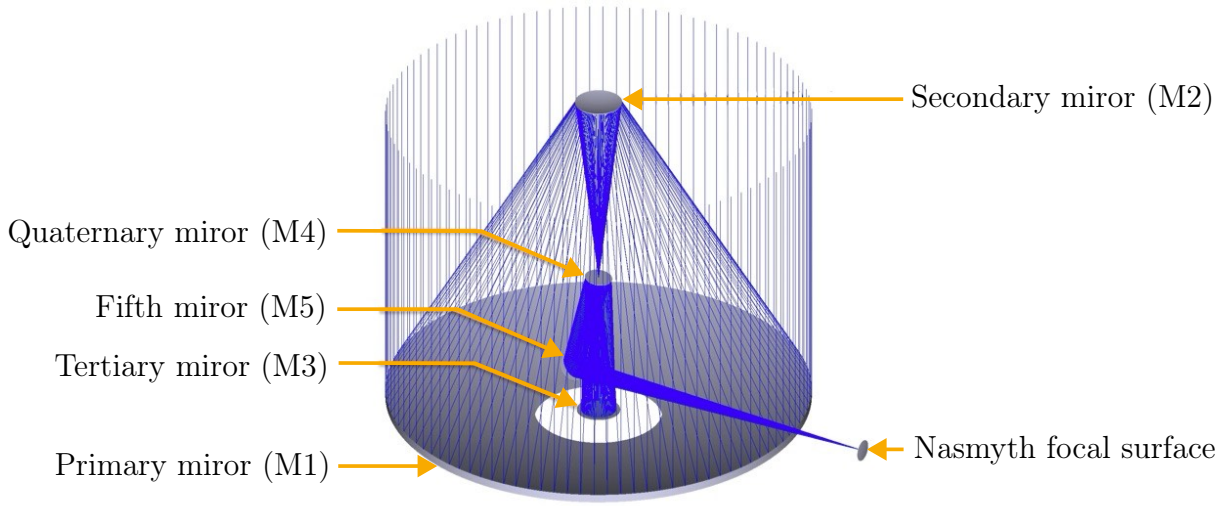

Figure 2.1: Optical design of the ELT [11].

Optics Relay For ELT Observations (MORFEO) that will not make observations by itself but will help to improve the performance of other instruments thanks to both natural and laser guide stars. This instrument will however only start to operate in 2032. Finally, the High Angular Resolution Monolithic Optical and Near-infrared Integral field spectrograph (HARMONI), a visible and near-infrared integral field spectrograph, the ArmazoNes high Dispersion Echelle Spectrograph (ANDES), a high resolution spectrograph working in the visible and near-infrared domains, and the Multi-Object Spectrograph (MOSAIC), that will enable spectrographic measurements in the visible and infrared for multiple objects at the same time in the widest FoV possible for the ELT, are for now scheduled to start operations between 2033 and 2034.

2.2 The METIS instrumental layout

The functional diagram of METIS optical system with all its optical components is represented in Figure 2.2.

As explained in [13] and [14], the light from the ELT will first pass through the Common Fore Optics (CFO) where it will be conditioned before entering the science modules. First of all, the light goes through a set of two Atmospheric Dispersion Compensation prisms in the first pupil plane in order to avoid the effects of atmospheric differential dispersion. The light will then go into a derotator in order to stabilize either the field or the pupil orientation within METIS. A pupil stabilization mirror will then ensure the pupil alignment between METIS and the ELT. The AO wavefront sensor will measure potential pupil displacements either due to the telescope or to the derotator to correct them in closed-loop.

At this point, the near-infrared light, *i.e.*, H and K bands (1.4 - 2.4 μm), will be sent to the adaptive optics subsystem by a dichroic filter. After that, a 2D beam chopper will enable to switch between the target and a reference sky in order to measure and subtract the thermal background. Finally, the second focal plane of the CFO will include two focal

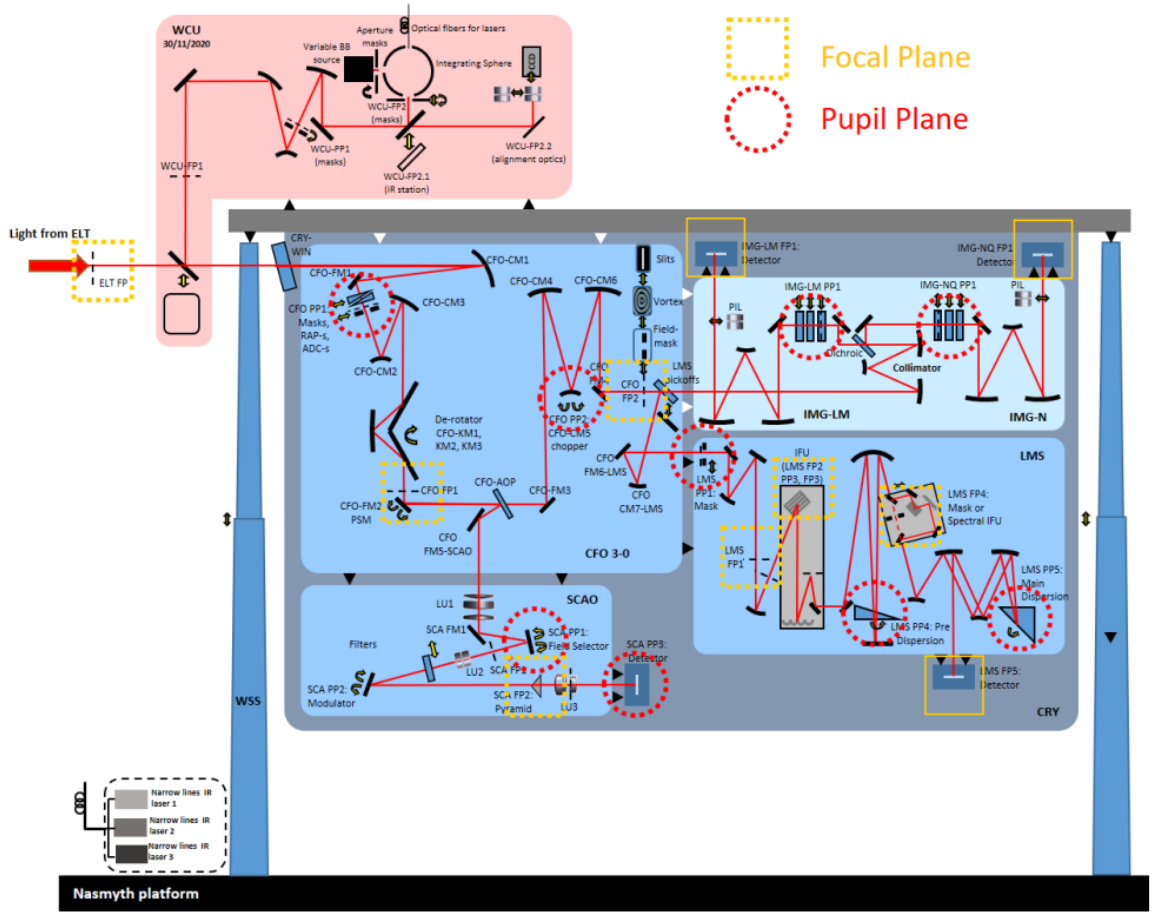

Figure 2.2: Conceptual set-up of METIS [13].

plane wheels featuring various field stops, slits, coronagraphic masks, alignment marks and a retractable beam splitter. When engaged, the beam splitter will direct the light into the spectrograph or send it to the imager.

The METIS AO system consists of a single conjugate AO system that will enable observations at or near the diffraction limit. As explained in section 1.4, this type of AO system uses the light of a single natural guide star in the near-infrared domain to measure the phase of the incoming wavefront through, in the case of METIS, a pyramid wavefront sensor that runs at a maximum loop frequency of 1 kHz. A tip-tilt mirror will enable field selection within the 27" field of view so that the guide star can be centered on the pyramid wavefront sensor. Another tip-tilt mirror will be used as a modulator in order for the light of the star to pass in the four quadrants of the pyramid. The maximum modulation radius associated to this modulator will be of $10\lambda/D$ which corresponds to 0.130" at the longest operating wavelength of the wavefront sensor.

Additionally, several filters will be placed on a filter wheel. Indeed, though the standard band at which the wavefront sensing is planned to perform in the K band, it can also work in H band. Moreover, a combined $H + K$ filter will enable to use fainter sources whereas a neutral density filter will enable to use bright sources without risking saturation. The wavefront will then be directly corrected by controlling the adaptive mirrors of the ELT, *i.e.*, M4 and M5.

As represented in Figure 2.2, METIS will integrate two science modules: an imager and a spectrograph. The wavelength range covered by the imager, *i.e.*, from L-band to N-band (3-13 μm), will be split in two channels (LM and N bands) that can be used in parallel. Before reaching the detectors, the light will first be collimated and then separated by a dichroic filter. At the pupil position, a set of filters, pupil masks and grisms could be inserted into the beams. A three mirror anastigmat will finally focus the light on the detector. As represented in Figure 2.3, the LM band imager covers a 10.50" square whereas the N band imager covers a 13.51" square.

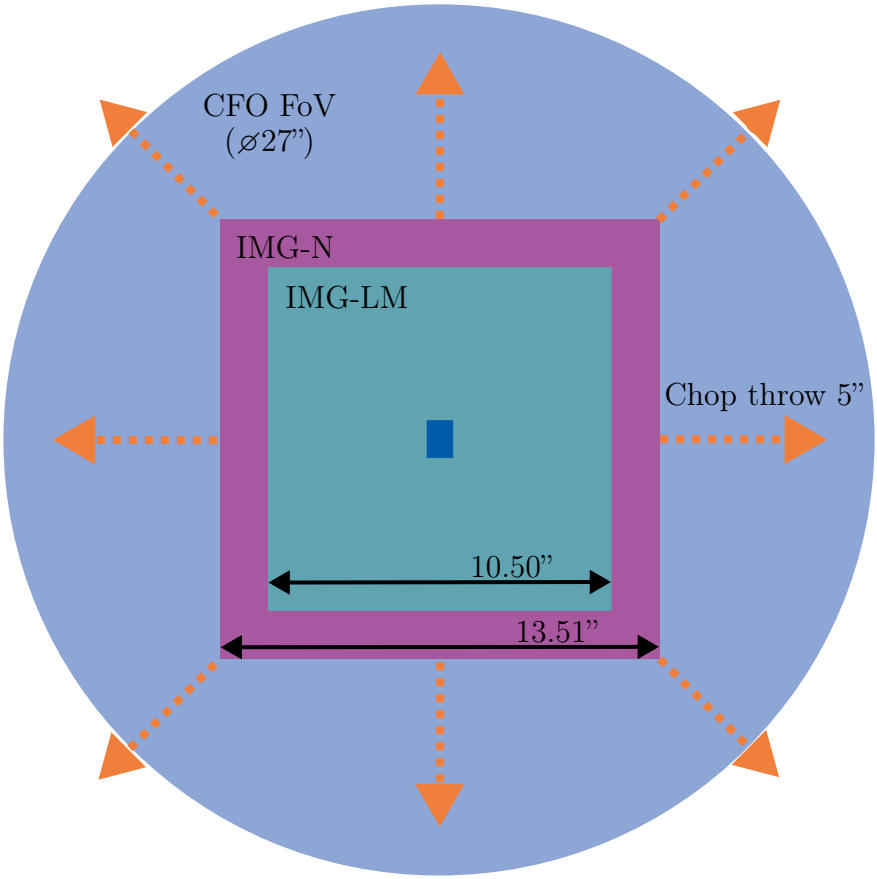

Figure 2.3: METIS fields of view. The larger FoV of the common fore-optics (indicated in light blue) allows chopper offsets of up to 5" in all directions as well as AO guide star pick-up within this field. The FoV of the LM- and N-band arms of the imager are shown in green and red, respectively. The FoV of the integral-field spectrograph is 0.58" × 0.93", shown here in the center. (Adapted from [14].)

Regarding the spectrograph, it will provide high-resolution ($R = 100,000$) integral-field spectroscopy at L and M bands on a 0.58" × 0.93" FoV. This field of view is re-arranged in 28 slices by a mirror slicer followed by a pre-dispersion prism. The main dispersion is then performed by a grating in the pupil plane. An extended wavelength coverage mode will also enable to project only three slices in the focal plane but providing a larger wavelength coverage of approximately 300 nm instead of 30 nm in the classical mode.

Finally, the warm calibration unit will provide several point sources to perform the various alignment and calibration tasks.

2.3 Performance of the METIS adaptive optics system

Simulations have been run to assess the performance of the METIS AO system [15]. The results as a function of guide star magnitude are shown in Figure 2.4. As shown in this figure, the highest loop frequency, *i.e.*, 1000 Hz, only delivers the best performance for stars brighter than magnitude 8. However, decreasing the loop frequency down to 500 Hz enables to use guide stars up to magnitude 12, and decreasing it down to 200 Hz allows to use stars potentially as faint as magnitude 13 to 14 but with a significative decrease of the performance.

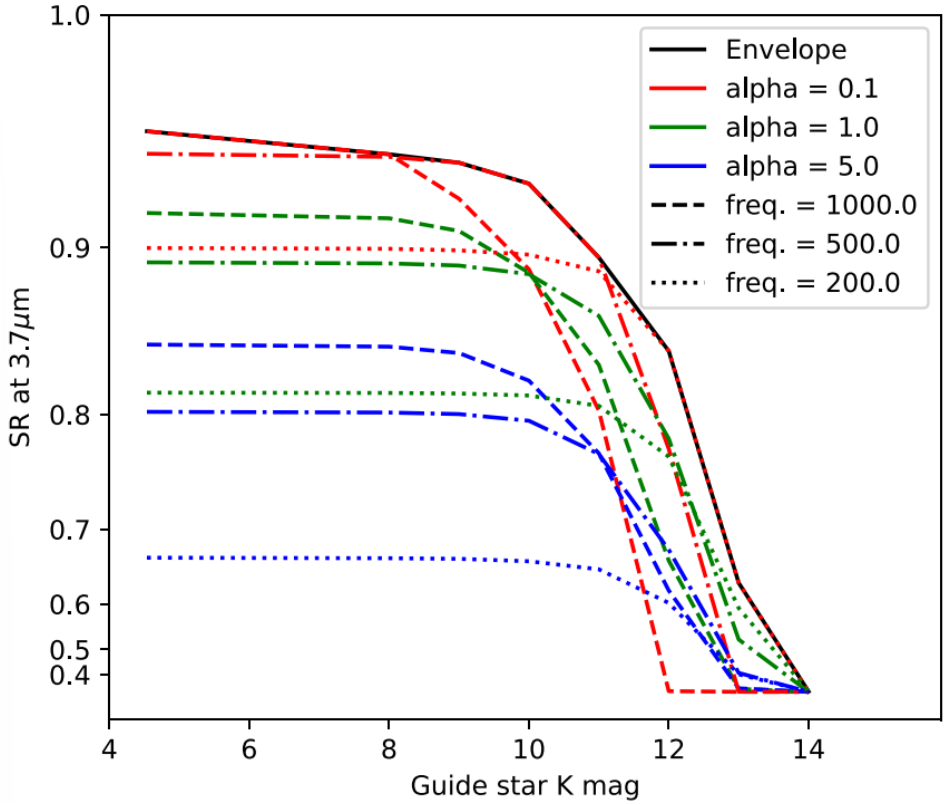

Figure 2.4: METIS AO system performance in terms of Strehl ratio as a function guide star K magnitude. The simulations were done for median seeing conditions at a zenith distance of 30°. The loop frequency and regularization strengths were varied according to the values mentioned in the legend [15].

Furthermore, as for any AO system, when there is an offset between the science target and the guide star, the performance of the correction is expected to decrease because of the effect of anisoplanatism. Nevertheless, as shown in Figure 2.5, the decrease in Strehl ratio remains acceptable for offsets up to approximately 18", therefore justifying the search for guide stars within a large part of the METIS field of view.

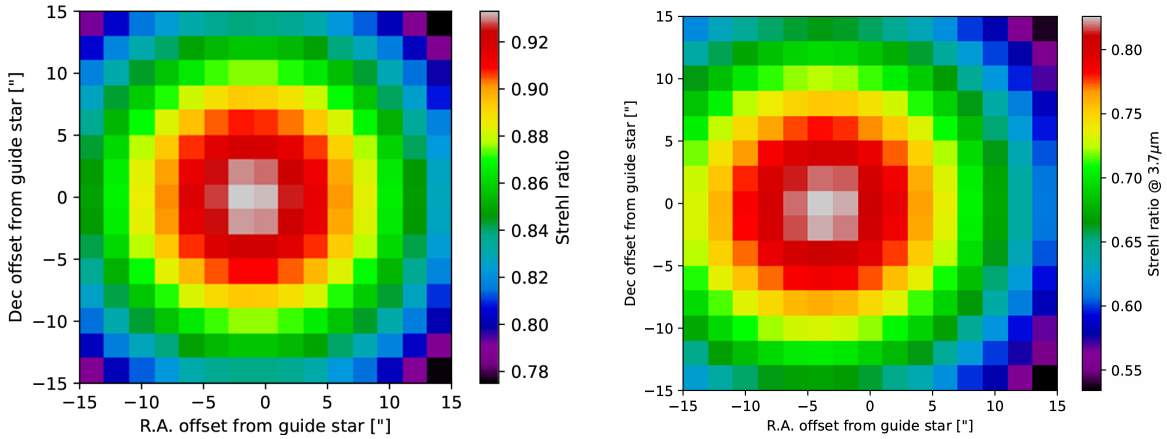

(a) $m_K = 10$ mag - $f = 1000$ Hz.

(b) $m_K = 12$ mag - $f = 200$ Hz.

Figure 2.5: Degradation of the Strehl ratio as a function of the distance to the guide star for a median seeing and $z = 30°$ [16].

In summary, METIS observations will be constrained by several limitations. As no laser guide star is planned at the beginning of operations, observations will be limited to targets for which a sufficiently bright star can be found in the field of view. Since this FoV has a diameter of only 27", this poses stringent constraints on the observability of extragalactic and solar system objects.

CHAPTER 3

REFERENCE SYSTEMS AND REFERENCE FRAMES

To determine whether stars lie within a few arcseconds of a solar system object, it is essential to accurately know their positions in the sky and their motions over time. Expressing these quantities requires to define a proper coordinate system. This chapter therefore aims to introduce the different coordinate systems used in this thesis.

First, the differences between reference systems and reference frames are recalled. Afterwards, the International Celestial Reference System and Frame are defined and their implementation in `Astropy` and `JPL Horizons` reviewed. The same explanations are then given for the Geocentric Celestial Reference System and Frame. These two descriptions are based on [17]. Finally, a brief description of the Jupiter System III and its implementation in `JPL Horizons` is given.

3.1 Difference between reference system and reference frame

Before describing the specific coordinate systems used throughout this work, it is necessary to clarify the distinction between reference systems and reference frames. A reference system is the complete specification of how a celestial coordinate system is to be formed. It defines the origin and orientation of the fundamental planes (or axes) of the coordinate system. It also includes some information about the models needed to construct the system and transform between observable quantities and reference data in the system. On the other hand, a reference frame consists of a set of identifiable points on the sky along with their coordinates, which serves as the practical realization of a reference system [17].

In general, the fundamental plane of a reference system corresponds to the extension to infinity of the Earth's equatorial plane at some date. As represented in Figure 3.1, the declination of an object is then defined as the angular distance north or south with respect to this plane whereas right ascension is the angular distance measured eastwards

from a reference point along the equator. This reference point is generally the vernal equinox, *i.e.*, the intersection of the ecliptic and equatorial planes, where the Sun passes from the southern to the northern hemisphere.

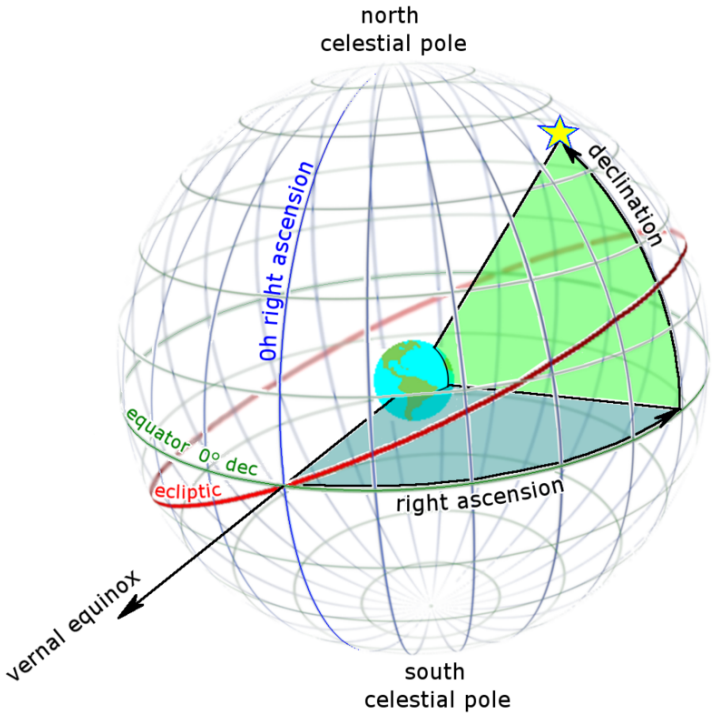

Figure 3.1: Right ascension and declination as seen from outside the celestial sphere [18].

Since these two planes are moving because of the precession and nutation of Earth's rotation axis as well as the intrinsic displacement of this axis across Earth's surface, such coordinate system must have a corresponding date, which usually is the epoch J2000 (January 1, 2000 at 11h58m56s UTC).

3.2 International Celestial Reference System and Frame

The first reference system commonly used to express celestial coordinates is the International Celestial Reference System (ICRS). This system is a right-handed inertial reference system whose origin is located at the barycenter of the Solar System whereas its axis directions are fixed with respect to distant objects of the universe. These axes are set in order to be kinematically non-rotating, and thus have no rotation, with respect to these reference objects. Its pole is pointing towards the Earth's north pole or, equivalently its fundamental plane is the Earth's equatorial plane whereas the reference direction is the vernal equinox. Finally, as for most reference system, its epoch is the J2000 epoch.

The realization of the ICRS is the International Celestial Reference Frame (ICRF). It is a set of 212 extragalactic radio sources measured with very long baseline interferometry. These sources have barely any intrinsic motion, which enable to use their coordinates to define the directions of the ICRS axes.

In `Astropy`, the `ICRS` class enables to give coordinates in this reference system assuming that the observer is at the Solar System barycenter. `JPL Horizons` also returns coordinates in this system but taking into account the observatory position. This has to be taken into consideration when using `JPL Horizons` data within `Astropy` functions. As represented in Figure 3.2, $p_{\texttt{Astropy}}$, the equivalent object position as seen from the Solar System barycenter, will be given by:

$$p_{\texttt{Astropy}} = p_{\text{JPL}} + p_{\text{obs}} \tag{3.1}$$

where p_{JPL} is the object position as given by `JPL Horizons` and p_{obs} is the observatory position at the observation time in the ICRS.

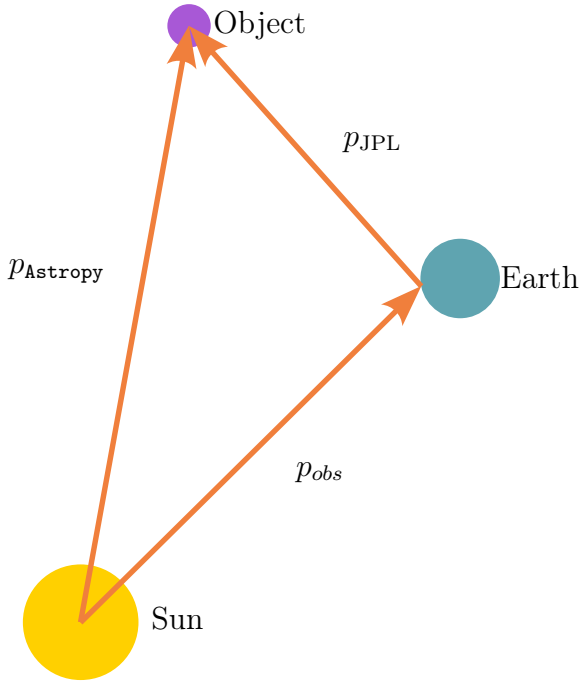

Figure 3.2: Relationship between the ICRS coordinates returned by `JPL Horizons` and those considered in the `ICRS` class of `Astropy`.

3.3 Geocentric Celestial Reference System and Frame

For Earth-based measurements it is also common to use the Geocentric Celestial Reference System (GCRS), an inertial reference system centered on Earth's center of mass. Once again, this system is kinematically non-rotating with respect to distant objects. Its orientation is determined by the one of the ICRS but this does not mean that it is the same as the one of the ICRS. For instance, the GCRS accounts for relativistic effects from the Sun and other solar system bodies while the ICRS does not. Transformation matrices are therefore required to convert the position of an object from one system to the other.

The Geocentric Celestial Reference Frame (GCRF) is the practical realization of the GCRS and therefore consists in a catalog of source positions whose coordinates are given

in the GCRS framework. In order for the orientation of the GCRS to be determined by the orientation of the ICRS, the GCRF is aligned with the ICRF.

This system corresponds to the `GCRS` class in `Astropy`. Note however that this class also enables to consider frames that are offset in both position and velocity with respect to Earth and thus to take into consideration the observatory position. Besides, this class also includes the observation time in order to take in consideration the variation of Earth's orientation.

3.4 Jupiter System III

Finally, for the particular case of observations of Jupiter's aurorae, another system has to be taken into consideration: the Jupiter System III [19]. This system is, as its name indicates, centered on Jupiter's center of mass. It also rotates with Jupiter's magnetic field and therefore has a sidereal spin period of 9.92 h. This characteristic enables the auroral ovals to be at fixed longitudes in this system. The Z-axis of this system is set by the spin axis of Jupiter whereas its X-axis is defined by a 0° latitude on the System III prime meridian, *i.e.*, $\lambda_{\text{III}} = 0°$. This meridian is defined by the Earth-Jupiter vector on a specific date in 1965.

As represented in Figure 3.3, the Y-axis can be set so that the system is left or right-oriented depending if one wants to have respectively increasing or decreasing longitude with time, as observed from Earth. Note that in the case of a right-oriented system, the latitude is then replaced by the colatitude $\theta_{\text{RH}} = 90° - \lambda_{\text{III}}$ and thus the X-axis is defined by a 90° colatitude on the system prime meridian.

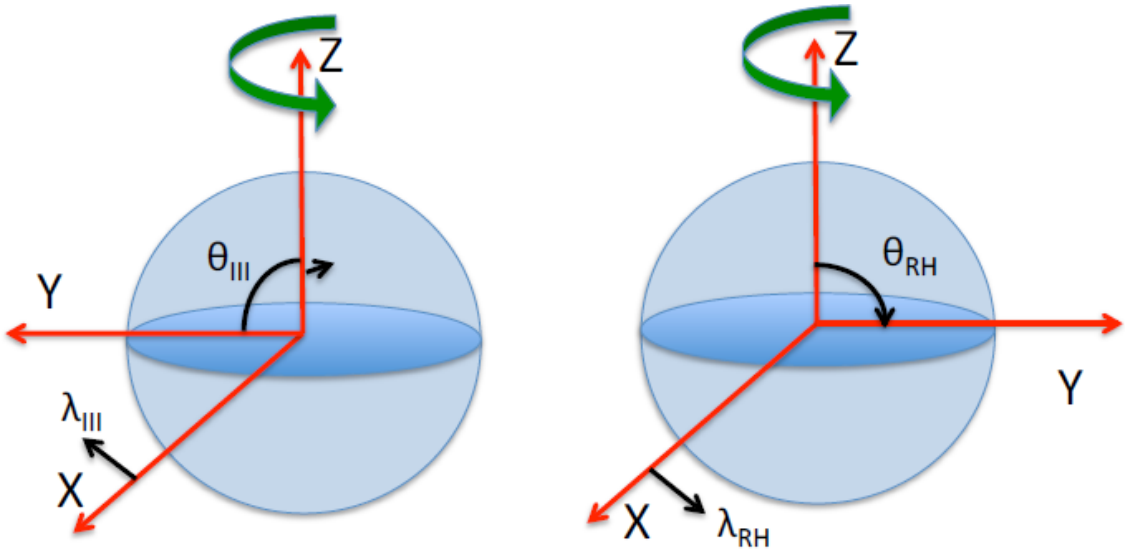

(a) Left-handed system where θ_{III} is the latitude and λ_{III}, the longitude.

(b) Right-handed system where θ_{RH} is the co-latitude and λ_{RH}, the longitude.

Figure 3.3: Representation of Jupiter System III [19].

In `JPL Horizons`, the longitudes and latitudes of Jupiter are provided in the left-handed system therefore meaning that the longitudes are increasing with time.

CHAPTER 4

SEARCHING FOR OFF-AXIS GUIDE STARS

This chapter focuses on describing the method followed for the determination of observation windows of solar system objects.

First of all, the basic requirements for a proper observation window are set. Then, the main principles of the tool developed within the framework of this project are described before detailing the different algorithms that make it up. The the principles of the search for suitable adaptive optics guide stars around the target are first given before describing the search for sufficiently long observation windows algorithm. Finally, the representation of the resulting observation windows is described and the time step used in the algorithms discussed.

Note that all the functions developed for this thesis are available in [20].

4.1 Requirements

In order for an object to be observable with METIS, several requirements must be fulfilled.

First, a sufficiently bright guide star must be present in the FoV. In the default case of an on-axis science target, the guide star must be located at a maximum of 13" from the region of interest on the science target in order to keep a 0.5" margin with respect to the edge of the 27" FoV. However, as represented in Figure 4.1, the target can also be observed off-axis which would enable to extend the radius around the target in which the guide star could be located. Because the science channels can be offset by a maximum of 5", any star located at 18" from the region of interest on the target can be used as a guide star. However, this configuration results in reduced operation capabilities. Indeed, it would restraint the directions in which chopping could be performed. Nevertheless this configuration has also been studied as it should enable to increase the number of windows in the most critical cases.

Given the Strehl ratio degradation presented in Figure 2.5, such separation would preserve a sufficiently high Strehl ratio for most solar system observation programs. In-

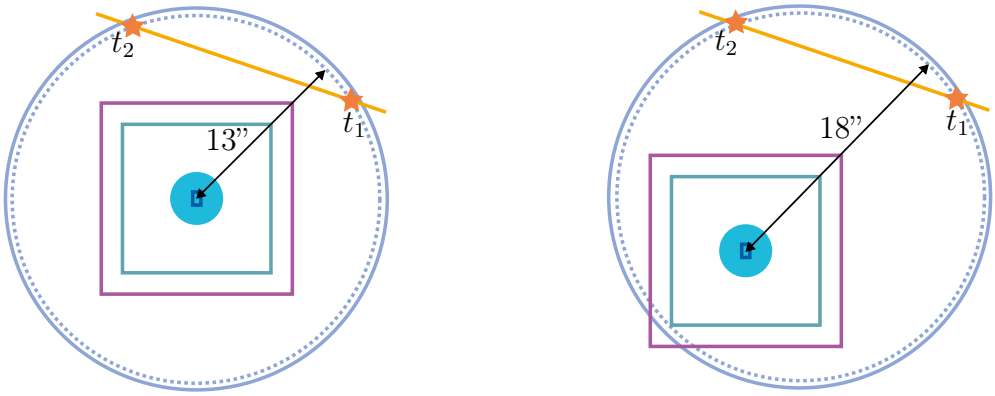

(a) Observation with the science channel centered in the CFO FoV.

(b) Observation with the science channel offset from the CFO FoV by the maximum amount (5”).

Figure 4.1: Illustration of on-axis and off-axis guiding on a solar system target. The blue circle represents the 27” FoV of the CFO and the dotted circle the 26” FoV in which guide stars can be acquired while keeping a 0.5” margin with respect to the edge of the CFO FoV. The squares illustrate the FoV of the IMG-LM (teal) and IMG-N (purple) arms while the small rectangular area corresponds to the FoV of the LMS. The potential observing window lasts from t_1 to t_2 for an observation of the center of the target represented in blue. (Adapted from [21].)

deed, for a guide star of magnitude 10 and a loop frequency of 1000 Hz, the Strehl ratio goes from 93 % on-axis to 82 % for an angular separation of 18” between the star and the target whereas it goes from 83 % to 63 % for a guide star of magnitude 12 and a loop frequency of 200 Hz.

Secondly, because solar system objects have a non-sidereal motion, the duration of their observations will be limited by the time spent by the guide star within the 13” or 18” FoV around the object of interest. For this thesis, in order to ensure a proper observation of the target, the minimum observation time has been set to 30 min. As a consequence, objects that would be so fast that they do not stay at least 30 min within METIS FoV would not be observable.

Concerning the guide stars, given the performances of METIS adaptive optics system described in section 2.3, they must be at least as bright as magnitude 12 in the K band in order to ensure that the correction is not too degraded. However, stars as faint as magnitude 13 or 14 have also been considered, though it would comes with reduced performance. Because it is one of the most complete catalog in this band, the Two Micron All Sky Survey (2MASS) catalog [22] will be used to determine the star positions and magnitudes m_K. This catalog however does not take into account the proper motion of the stars.

Moreover, METIS AO system has a 2” diameter field stop in order to reduce contamination by the light from another object. Therefore a separation of at least 1” between the guide star and the science target will prevent any straylight that would degrade the AO performance. This constraint is however less critical if the target is fainter than the

guide star and a 0" separation could be acceptable.

Additionally, other requirements specific to some objects have to be taken into consideration. For example, for moons, their separation with respect to their parent planet has to be sufficient to avoid any straylight contamination whereas for Jupiter's aurorae, specific longitudes in Jupiter System III coordinate system are required to observe a specific auroral oval. Finally, for comets, as they are more active when they are close to their perihelion, a requirement on the heliocentric distance can be necessary.

Finally, the object must have a sufficient elevation and the Sun be sufficiently low to enable to proper observation.

4.2 Observability assessment tool principles

The principles of the tool developed for this thesis are illustrated in Figure 4.2. The first step that has to be performed is the search for stars around the object. This search relies on several external resources. First, `Astropy` [2, 3] or `JPL Horizons` [4] are used to determine the object position. After that, since the star magnitude in K-band is required, the 2MASS catalog of the VizieR database at Centre de Données astronomiques de Strasbourg is queried to determine if there are stars around the object [22, 23]. At the end of the search for stars, the resulting data are stored in a newly created `WindowData` structure. This structures can then be used to perform the search for sufficiently long windows or directly to obtain a representation of the possible observation windows.

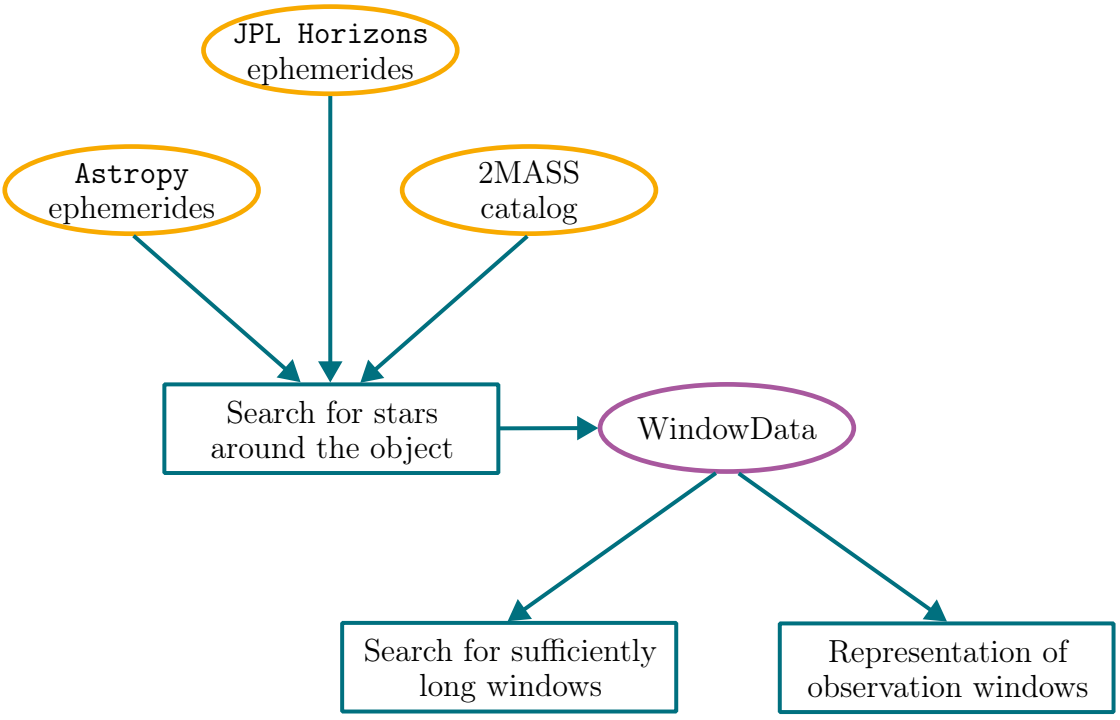

Figure 4.2: Main principles of the tool developed to asses the observability of a solar system object. Orange ovals represent external resources, teal boxes, functions developed as part of this thesis and the purple oval, the custom data structure used to store observation results.

4.2.1 Search for stars around the target

The main principles of the search for stars around the targets are summarized in Figure 4.3.

As represented in this figure, for times separated by a time step Δt between t_0 and t_{end}, the `search_stars_around_object` function first checks that the Sun is sufficiently low with respect to the horizon to enable a proper observation of the target. This is done with the results in GCRS system returned by the `get_sun Astropy` function. For METIS observations, the boundary has been set to a maximum elevation of 18° in order to observe during the astronomical night [24].

The observability of the target is then verified by ensuring that it is at least 30° above the horizon to avoid too much atmospheric extinction. This information about the target can be acquired by querying the `JPL Horizons system` through `Astroquery` [25], or if the target is a planet or Pluto, by the `get_body` function of `Astropy`. Both of them take the observer position into consideration, therefore determining the target elevation at a specific observatory in the GCRS coordinate system. They also consider the light travel time, t_{light}, from the body to the observer so that the position returned at a given time, t, is the target apparent position, *i.e.*, the target position at time $t - t_{\text{light}}$.

The target must also be sufficiently slow to stay inside the 27" field of view during at least the minimum duration of an observation, typically 30 min. This is done by verifying that:

$$\theta_{t_i, t_{i+T_{\min}}} < 27'', \tag{4.1}$$

where $\theta_{t_i t_{i+T_{\min}}}$ is the angular distance covered by the object center between times i and $i + T_{\min}$ as seen by the observer, and $T_{\min}$ is the minimum duration of a window. As this involves an apparent motion, GCRS coordinates were used.

If the target is an asteroid or a planet, the presence of at least one background star within the field of view is directly verified. On the other hand, if the target is a moon, it is first necessary to check if the separation between the moon and its associated planet is sufficient enough to avoid any contamination from the planet light. This distance is set by default to 0" but has been extended to 13.5" and 27" for this study in order for the planet to always remain outside the field of view of the instruments and avoid any straylight. In this case, the planet position is retrieved through the `get_body` function of `Astropy`. The condition to be satisfied is thus:

$$\theta_{\text{moon}_{\text{center}}, \text{planet}_{\text{center}}} - \theta_{r,\text{moon}} - \theta_{r,\text{planet}} > \theta_{\min}, \tag{4.2}$$

where $\theta_{\text{moon}_{\text{center}}, \text{planet}_{\text{center}}}$ is the angular separation between the centers of the moon and the planet, $\theta_{r,\text{moon}}$ and $\theta_{r,\text{planet}}$ respectively are the angular radius of the moon and the planet and $\theta_{\min}$ is the required minimum angular separation.

The search for stars around the object is performed in the 2MASS catalog through the `conesearch` function of the `Astroquery` package. Since the `conesearch` function performs the search for stars in the Sun centered ICRS coordinate system, there will be some parallax effect when considering an observer location on Earth. It is thus necessary

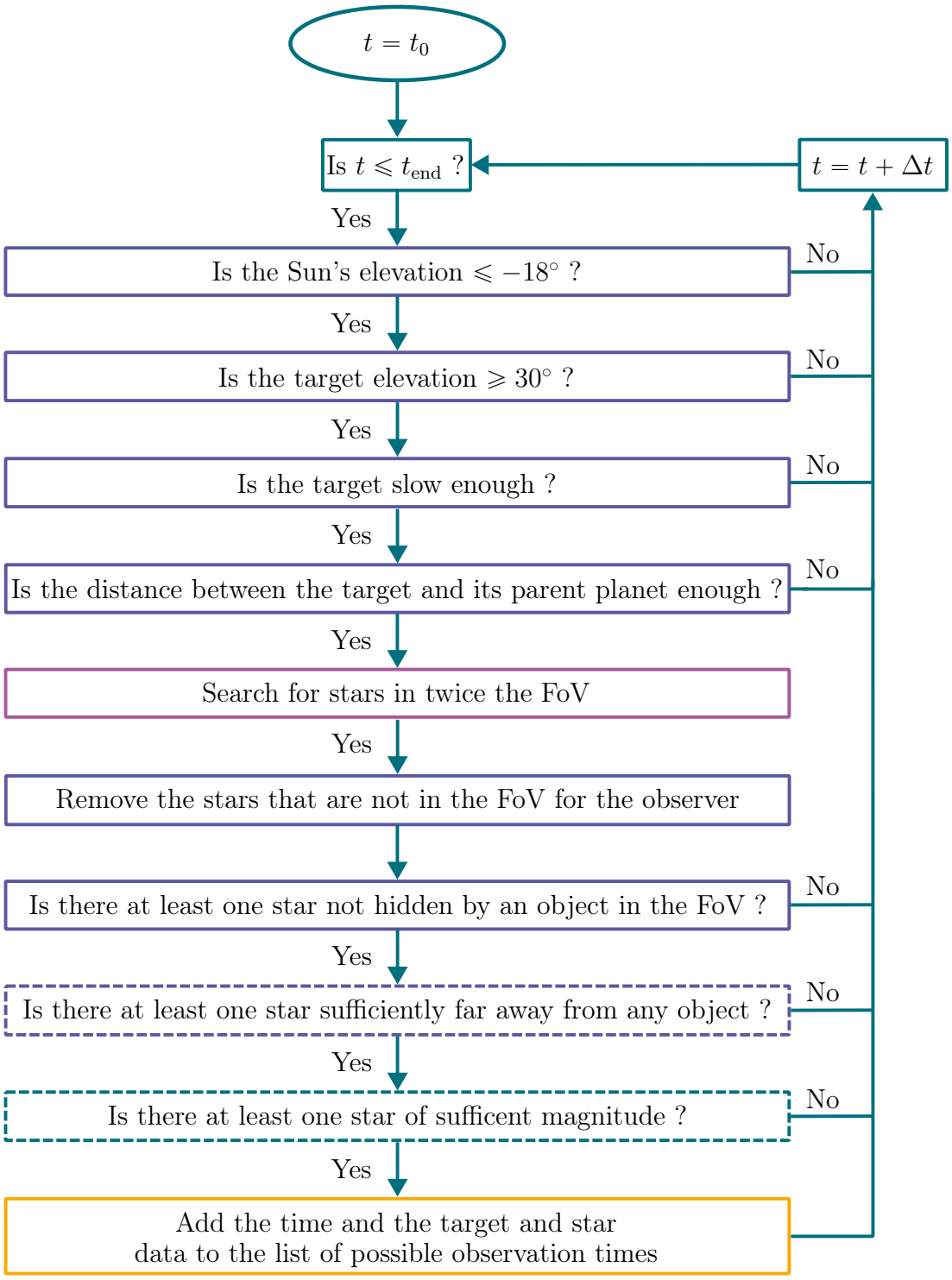

Figure 4.3: Block diagram of the search for times when there are stars around the science target. Dotted lines represent optional filtering steps. Dark blue and purple boxes indicates steps respectively performed with data in the GCRS, ICRS.

to introduce a factor 2 on the radius of zone within which the search is performed and then to remove from the list the stars that are not within the desired FoV as seen from the observer location in the GCRS system. For this work, the desired FoV has always been considered equal to 18" and the data for the 13" FoV has been retrieved afterwards by keeping the stars within this smaller FoV.

As represented in Figure 4.4, three configurations of the target can be used:

- *limb*, where at least a portion of the target must lie within 13" or 18" of the guide star at any given time. Note that this portion of the limb is not fixed throughout the observation window, as the target moves with respect to the star,
- *center*, where the target center must be within 13" or 18" from the guide star,
- *full*, where the entire target must lie within 13" 18" from the guide star.

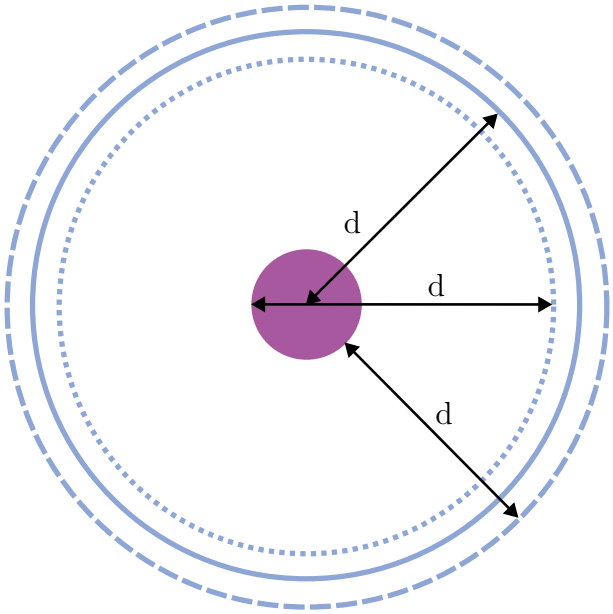

Figure 4.4: Representation of the three possible configurations of the search region around the target. The purple circle corresponds to the target and the dashed, plain and dotted circles respectively indicates the limit of the search region in the *limb*, *center* and *circle* configurations.

Finally, it is necessary to verify that, as seen by the observer in the GCRS coordinate system, the stars are not hidden by the target and the parent planet if any. Note that in all cases, these objects are considered perfectly spherical. Besides, a minimum separation between the star and the target and potential associated planet can be imposed. This distance is set to 0" by default but has been considered equal to 1" in order to prevent any straylight that would degrade the AO performance. As this constraint could however be relaxed if the target is fainter than the guide star, and though the results are not explicitly written in this report, the case of a 0" separation also has been studied.

Note that it is also possible at this step to already filter stars that are too faint, though for this work, this filtering has been performed during the search for sufficiently long windows. Additionally, it is also not necessary to already impose a particular separation between the object and its parent planet as the default value of 0" will ensures that the target is not hidden by the planet. More restrictive separation criteria can then be applied during the search for sufficiently long windows. The same is also true for the separation between the star and the target and, if there is a parent planet, for the separation between this planet and the star.

At the end of the algorithm, a `WindowData` structure containing the following information is returned:

- times for which stars have been found around the target,
- star positions at these times,
- star magnitude at these times and positions,
- target (and parent planet if any) position at these times,
- target (and parent planet if any) angular radius at these times,
- target longitude in Jupiter System III if the target is Jupiter,
- the different parameters used for the search: time step, FoV radius, minimum observation duration, maximum magnitude, ephemeris system used, margin around object (and parent planet if any) and separation between the target and its parent planet if relevant.

4.2.2 Search for sufficiently long windows

Once stars have been identified around the target for different times during the observation period, it is necessary to verify if they remain in the FoV for a sufficiently long time. The principles of the `compute_observation_windows` function enabling this search for observation windows are given in Figure 4.5.

As represented in this figure, for comets, it is possible to filter the data obtained with `search_stars_around_object` in order to keep only the times for which their heliocentric distance is smaller than a given distance, typically 1.5 AU to ensure that they will be sufficiently active.

On the other hand, if the target is one of Jupiter's auroral ovals, it is necessary to check that Jupiter's orientation with respect to Earth enables to observe the main part of the aurora.

Then, if the target is a moon, and if not already done in the search for guide star, the times for which the separation between the moon and it associated planet is not sufficient are removed from the data set. In a similar way, the times for which the star is too close to the target or its associated planet, if any, can be removed if not already done during the search for guide stars.

Afterwards, the different windows are separated and, for each possible windows, only

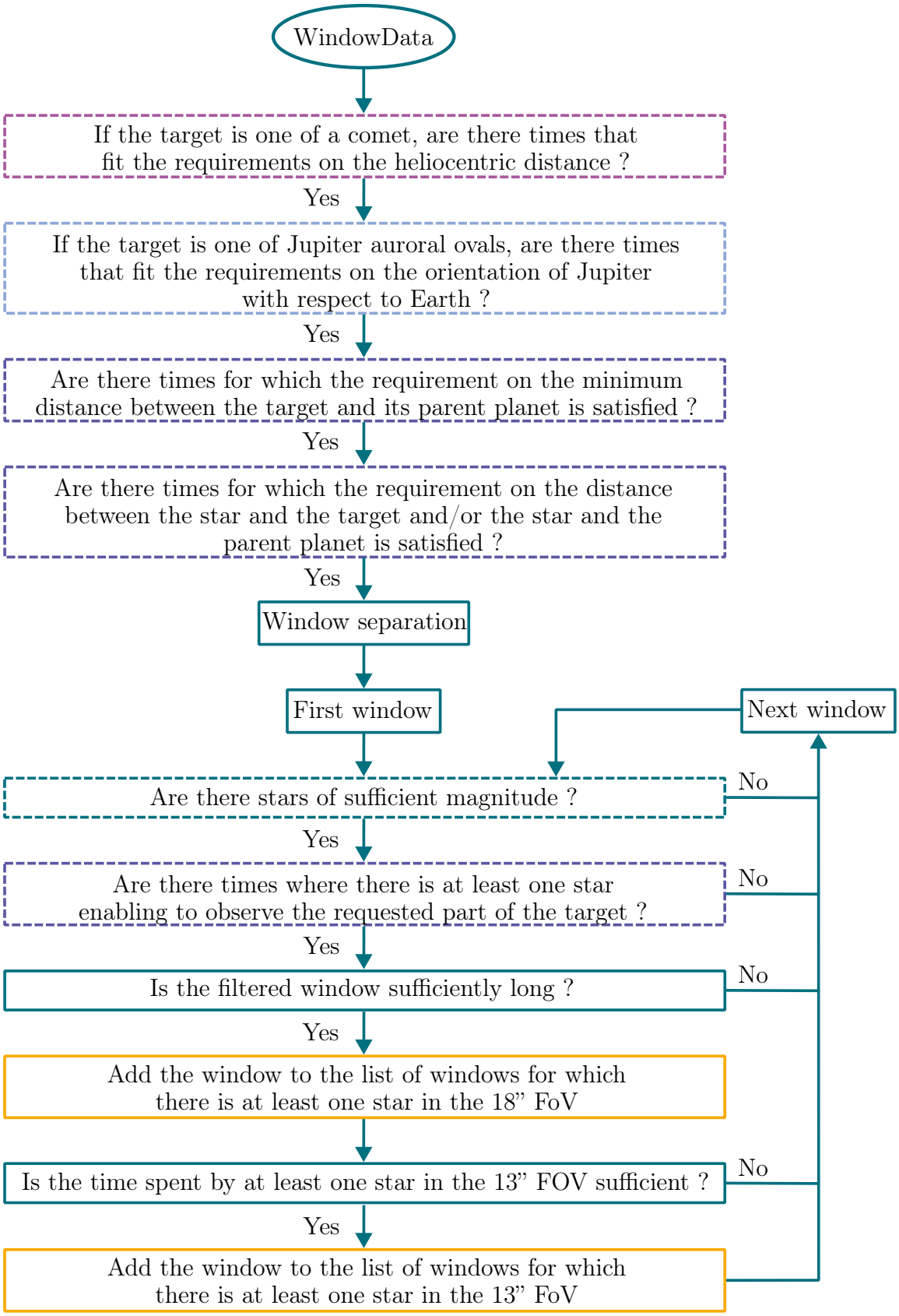

Figure 4.5: Block diagram of the search for sufficiently long windows. Dashed lines represent optional filtering steps. Dark blue, purple and light blue boxes indicates steps respectively performed with data in the GCRS, ICRS and Jupiter System III.

the data of sufficiently bright stars are kept if the faintest stars were not already filtered during the search for stars around the object.

For the biggest objects such as planets, it is then possible to keep only the stars that enable to observe a part of the object located between specific latitudes. Two options are possible:

- *part*, where at least a fraction of the zone comprised between the specified latitudes has to be within 13" or 18" from the guide star,
- *zone*, where the full zone comprised between the specified latitudes has to be within 13" or 18" from the guide star.

The time spent by the star that remains the longest in the 18" FoV is then compared to the minimum required observation time. If it is larger, the observation window is retained. Finally, in order to determine if the object could be kept at the center of the 27" FoV, which would facilitate chopping operations, the time spent by the star that remains the longest in a FoV of 13" around the position of interest on the target is compared to the required observation time. If it is longer, the observation window is added to the list of windows enabling the object to stay at the center of the field of view.

Note that if multiple guide stars are present within the 18" region around the object, the one corresponding to the longest observation window is selected. In cases where several guide stars remain within the region for the same duration, the one closest to the object is considered.

The algorithm then returns the number of windows for which there is at least one star in the 13" and 18" field of views, the beginning and duration of these windows and the magnitude of the guide star. These results can then be used in the `plot_mag_vs_obs_time` function to plot the different window durations as a function of the star magnitudes.

4.2.3 Representations of observation windows

The `plot_star_trajectory_wrt_obj` function uses the same principles as the `compute_observation_windows` function to determine if an observation window is sufficiently long and returns, for all observation windows of the data set, a graph similar to the one given in Figure 4.6.

In these plots, the target is represented by a purple circle of radius corresponding to the angular radius of the target at the time of the observation. Light blue circles corresponds to the 18" region in which stars can be located whereas the dark blue circles corresponds to the 13" region. Solid circles denote a 13" or 18" distance from the target center, dashed circles correspond to 13" or 18" from the object limb and dotted lines indicate the limit of the 13" or 18" region enabling to observe the entire target. In the case where a zone of interest is defined, purple dashed lines represent the limits of this zone.

Star trajectories are represented in orange with little stars and time indications at the beginning and end of the window as well as when the star enters or exits the 13" region. Solid orange lines correspond to moments when the star is within 13" from the object

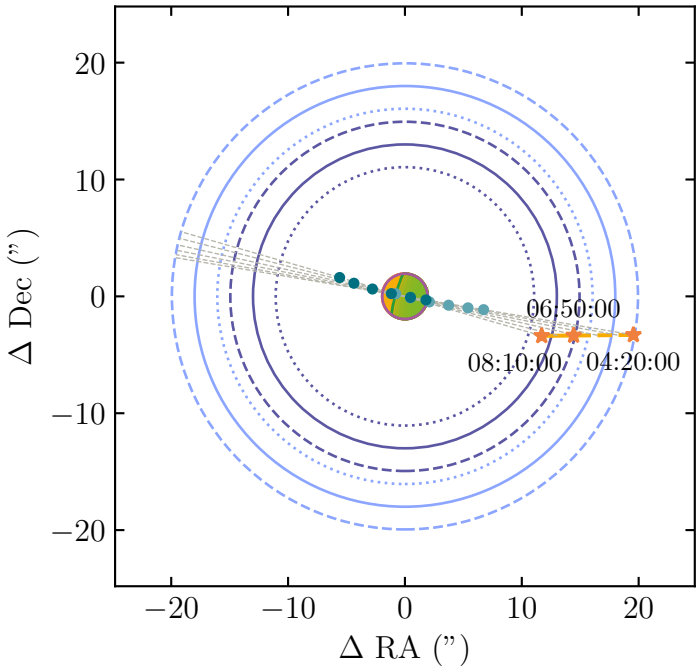

Figure 4.6: Example of representation of observation windows - Uranus observation window of November 25, 2032 - $m_{\mathrm{K,\,min}} = 12$ - $\Delta t = 10$ min - `Astropy` ephemerides.

whereas dashed lines indicates times when the star is outside the 13" region. Teal points indicate the closest point on a circle centered on the star, at a given time, to the target center. Light teal points correspond to a 13" circle, while dark teal points correspond to an 18" circle. These points are thus an indication of which part of the target is observable at a given time.

Finally, the part of the target that is within 13" or 18" from the guide star is represented respectively in green and orange. Note that a superimposition effect enable to determine if a specific zone remain within the 13" or 18" range from the star during the whole window or during only a part of it. However, this does not take into consideration the field of view of the scientific cameras of METIS and therefore does not correspond to the observability of the full target. For example, provided that the object is not larger than the FoV of the camera, a part of the object that is further than 13" or 18" from the guide star would still be observable.

4.2.4 Time step

A crucial parameter for this study is the time step Δt between two star searches around a target. On one hand, the smaller the time step, the more precise the estimation of the window duration will be. On the other hand, a too small time step will considerably increase the computation time. After a few trials it appeared that, for most of the targets, a time step of 10 min was a good compromise between computation time and

results accuracy. Indeed, for many targets, observation window computations can last several hours. With such a time step, the search for stars around the target over a one year period approximately takes 1 h. However, for targets with a fast apparent motion such as inner solar system planets, main-belt asteroids or some comets, a time step of 5 min was preferred. Indeed, as illustrated in Figure 4.7, with such fast objects, several windows could be considered as too short if a 10 min time step was used.

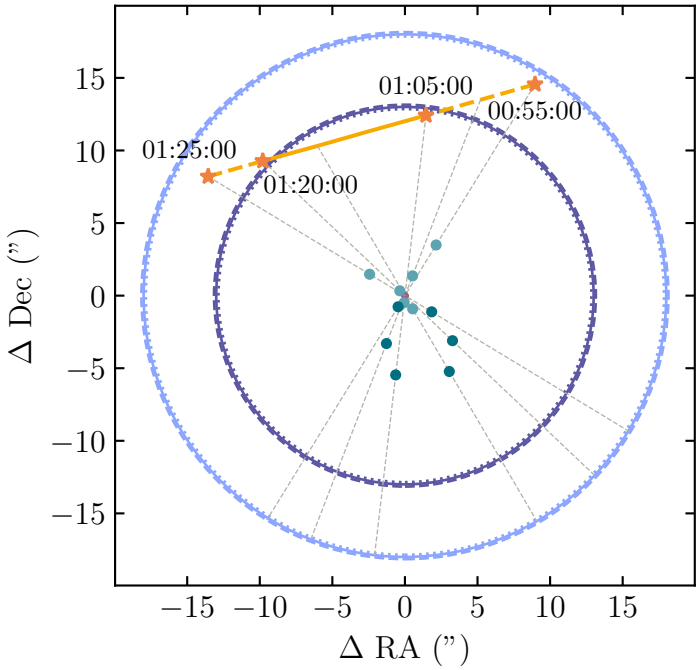

Figure 4.7: Hygiea observation window of July 23, 2034 - $m_K < 12$ - $\Delta t = 5$ min - JPL ephemerides.

Another effect of the time step is the fact that, if it is too large compared to the target apparent motion, observation windows for which the star is eclipsed by the object may not be detected properly as represented in Figure 4.8. This especially happens for inner solar system planets as they are fast objects of large angular size.

However, further decreasing the time step would lead to too long computation time and, after inspection, for small targets, only one or two windows are affected by this phenomenon. The default time steps were thus kept equal to 10 min for distant objects and 5 min for closer ones. However, as it will be shown in the next section, there are only a few windows for inner solar system planets. Since these targets are more likely to have undetected windows for which the star is eclipsed by the target, all the windows that were found will be reexamined with a time step of 1 min.

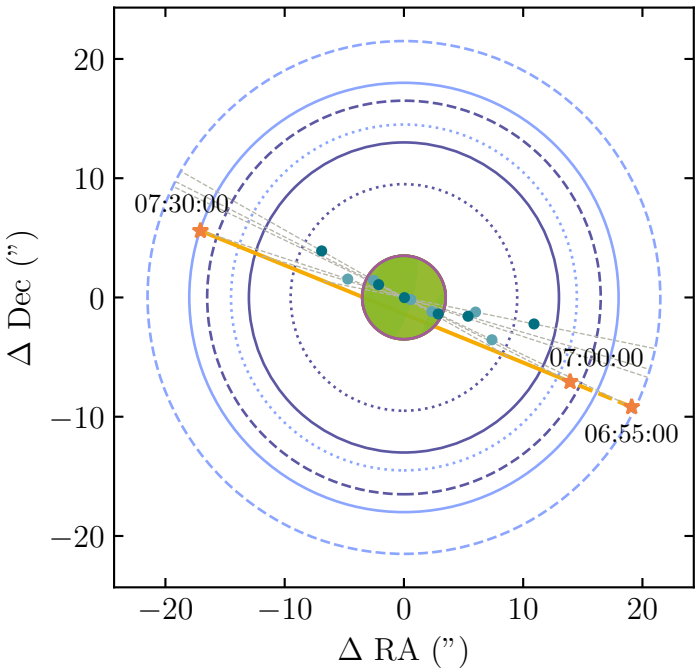

Figure 4.8: Mars observation window of January 23, 2031 - $m_K < 14$ - $\Delta t = 5$ min - JPL ephemerides.

CHAPTER 5

RESULTS OF THE SEARCH

In this chapter, the code developed for this thesis is tested on different potential targets. In order to assess the feasibility of observations on diverse solar system objects, different targets of various orbits and sizes have been selected and their associated results analyzed:

- Venus and Mercury, planets within Earth's orbit,
- Uranus and Mars, planets beyond Earth's orbit
- Vesta and Hygiea, respectively inner and outer main-belt asteroids,
- Pluto, a prototype for TNOs,
- 67P/Churyumov–Gerasimenko, a Jupiter familly comet,
- C/2024 E1 (Wierzchoś), a dynamically new Oort cloud comet,
- C/2014 UN271 (Bernardinelli–Bernstein), the largest Oort cloud comet known whose orbit will remain far from the Earth,
- Io, Jupiter's innermost Galilean moon,
- Jupiter, and more precisely its aurorae.

Since the first light of the ELT is scheduled for 2030, the search for observation windows has been performed between January 1, 2030 and January 1, 2036 for all targets except for C/2024 E1 which is not anymore observable from Chile at this period. It has thus been studied between January 1, 2025 and January 1, 2031. Note that during this period, the comet also reaches its perihelion.

Finally, the influence of the required star brightness and position with respect to the target are studied.

5.1 Planets

Concerning the observations of planets, it appeared that observations of Mercury are not possible as it never reaches a 30° elevation because it is close to the Sun. The limit on

the planet elevation should be lowered below 20° and the one of the Sun raised up to −6° to be able to observe Mercury for 30 min but even then, the planet would be too fast to stay in the 27" FoV of METIS during the whole observation.

The case of Venus is similar as this planet is never above 30° when the Sun's elevation is below −18°. However, there are some moments where its apparent velocity would be slow enough to enable a 30 min observation window. Indeed, decreasing the minimum planet elevation to 20° would lead to 1 possible window of 30 min if only stars brighter than magnitude 12 are kept, 2 windows if this limit is extended to magnitude 13 and 3 windows if it is extended to magnitude 14. However, as Venus has a large angular size, these windows would only enable to observe a part of it and since this planet has a high apparent velocity, the part of Venus within 18" from a guide star would not always be the same during the observation.

Regarding planets farther from the Sun than the Earth, as shown in Figure 5.1, there are a few windows enabling to observe Mars. If the guide star must be brighter than magnitude 12, 7 windows enable to observe at least a part of the planet. As the search was performed over six years, this corresponds approximately to an average of one window per year. Extending the acceptable stars to those of magnitude 13 or 14 enables to increase the number of windows to 13 or 24. However, these windows are very short and none of them enables to have a star within 18" from the entire planet during 30 min. Nevertheless, since these windows occur when Mars is near its maximum distance from Earth, the planet angular diameter is smaller than 10" so that the whole planet can still be in the field of view of the imagers. Note also that, in this figure and in all the following scatter plot, points corresponding to guide stars between 0 and 13" from the target indicates that the star is located in this region during at least 30 min but the window duration reported in the plot is the one of the whole window.

Figure 5.2 illustrates one of these observation windows. As visible in this figure, for Mars, during a 30 min window a given part of the object is not always within 18" from the guide star. This is explained by the high apparent motion of this planet which makes it move fast with respect to the guide star.

This difficulty to observe inner planets was expected as it was already shown in [21] that there was no suitable windows for Mercury and Venus and only a few for Mars.

Regarding Uranus, as shown in Table 5.1, there are many more potential observation windows including some where the whole object can be observed in the 18" FoV or even sometimes in the 13" FoV. As represented in Figure 5.3, these windows are much longer than for Mars mainly because of a much slower apparent motion due to its smaller orbital velocity and larger distance to the Earth. This larger distance also explains the fact that about two third of the windows enable to observe the whole planet. Indeed, such large distance leads to a small angular radius for the planet and it is therefore much easier for the whole planet to stay within 18" from a guide star for a few hours.

From Table 5.1 it can also be seen that, as expected, `Astropy` and `JPL Horizons` ephemerides of Uranus yield almost the same number of windows, differing by only one in some cases. Besides, as illustrated in Figure 5.4, in some cases, a given window can

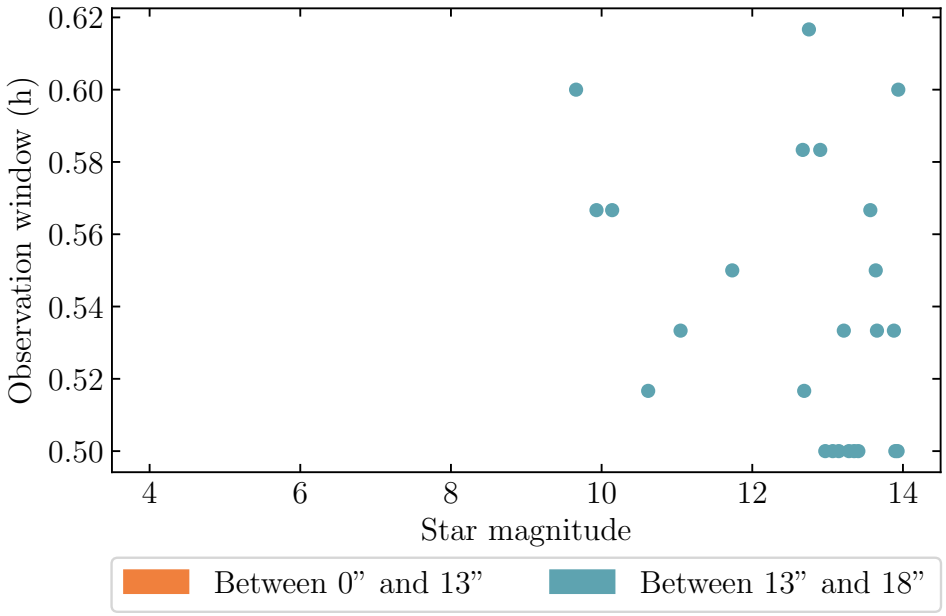

Figure 5.1: Scatter plot of observation window duration as a function of guide star magnitude for windows in which at least a part of the limb of Mars is observable - $\Delta t = 1$ min - `Astropy` ephemerides.

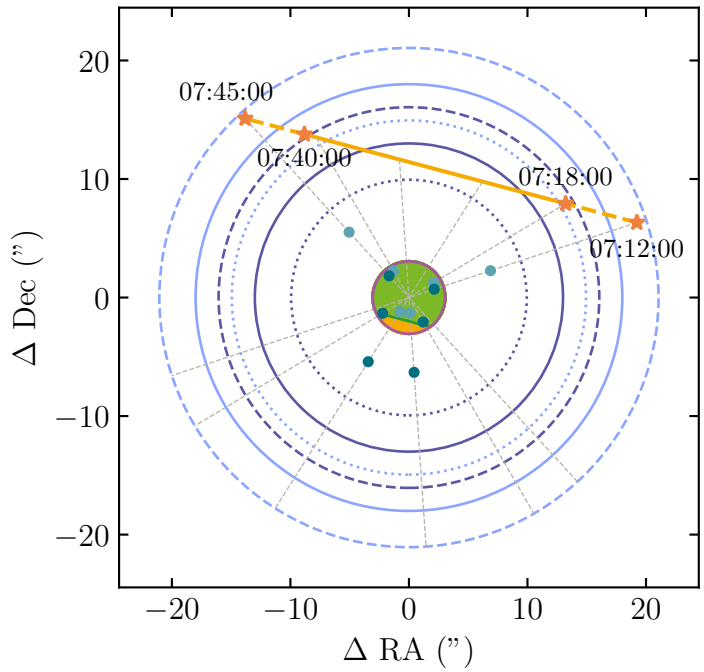

Figure 5.2: Mars observation window of February 3, 2033 - $m_K < 12$ - $\Delta t = 1$ min - `Astropy` ephemerides.

be a few minutes longer or shorter depending on whether the planet position has been obtained through `Astropy` or `JPL Horizons`. This can be explained by the different numerical methods used by the two systems to compute the ephemerides of an object. Indeed, though both compute ephemerides based on the DE440/441 model, `JPL Horizons`

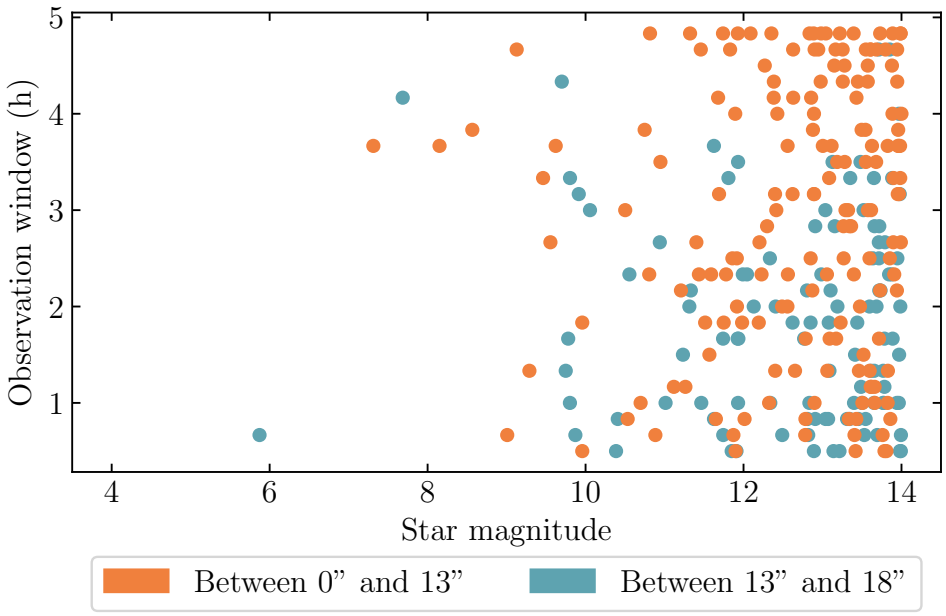

Figure 5.3: Scatter plot of observation window duration as a function of guide star magnitude for windows in which at least a part of the limb of Uranus is observable - $\Delta t = 10$ min - `Astropy` ephemerides.

Table 5.1: Number of observation windows of at least 30 min for Uranus in different configurations - $\Delta t = 10$ min - `Astropy` and `JPL Horizons` ephemerides.

Region of interest	Maximum separation to guide star	`Astropy`			`JPL Horizons`		
		$m_{\mathrm{K,\,min}}$			$m_{\mathrm{K,\,min}}$		
		12	13	14	12	13	14
Target limb	18”	87	149	278	86	148	277
	13”	51	93	170	52	93	171
Target center	18”	77	129	233	76	128	232
	13”	40	71	137	40	71	136
Entire target	18”	61	104	198	61	104	198
	13”	28	52	105	29	53	107

directly integrates the equations of motion with initial conditions adjusted to fit actual position measurements whereas `Astropy` interpolates between JPL results contained in an ephemeris file [4]. Results obtained with `JPL Horizons` should thus be more accurate though using these ephemerides increases the computation time by 5 to 10 min for the search for observation windows over one year. However, as the computation time with `Astropy` for a one year period was of approximately 1 h, this increase is not too problematic as long as a reasonable search period is used. Note also that with `JPL Horizons`, if the time step is too small, it is necessary to divide the search period in smaller periods as the number of ephemerides that can be returned at the same time by the `JPL Horizons`

system is limited. Nevertheless `JPL Horizons` ephemerides are used in the rest of the study.

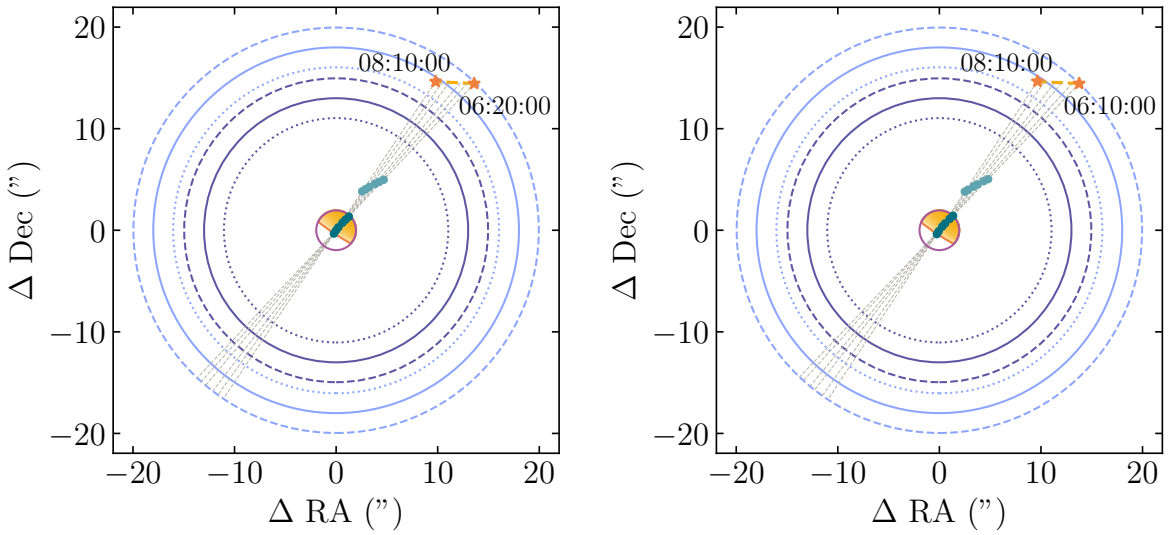

(a) `Astropy`. (b) `JPL Horizons`.

Figure 5.4: Differences between Uranus observation windows of December 4, 2034 obtained with `Astropy` or `JPL Horizons` ephemerides - $\Delta t = 10$ min.

Moreover, it appears that the limiting factor for the duration of observation windows on Uranus are its elevation as well as the one of the Sun. Indeed, as illustrated in Figure 5.5, for most of the longest windows, the guide star could still be used as guide star before the beginning of the window or after its end if the conditions on the target and the Sun elevation were met.

5.2 Main-belt asteroids

Concerning the main-belt asteroids, as visible in Table 5.2, the number of windows enabling to observe Hygiea is of the same order of magnitude as for those enabling to observe Uranus. However, as visible in Figure 5.6, these windows are much shorter with a maximum duration of 1 h 20 min. This is due to the much larger apparent motion of such objects which does not enable a guide star to remain within 18" from the object for several hours.

As for Mars, the duration of the observations of main-belt asteroids is thus mainly constrained by their apparent velocities. As Hygiea is an outer main-belt asteroid, its apparent motion is slower than for an inner main-belt asteroid of similar orbital parameters except for their semi-major axes and position on their orbit. It is therefore expected that the opportunities for observing main-belt asteroids will vary according to their position in the main belt, with more and longer observation windows for asteroids located farther from the Sun. Conversely, the closer an asteroid is to the Sun, the more its apparent velocity is similar to the one of Mars and there will be fewer available observing windows, and shorter durations for each of them. This phenomenon is further confirmed by the

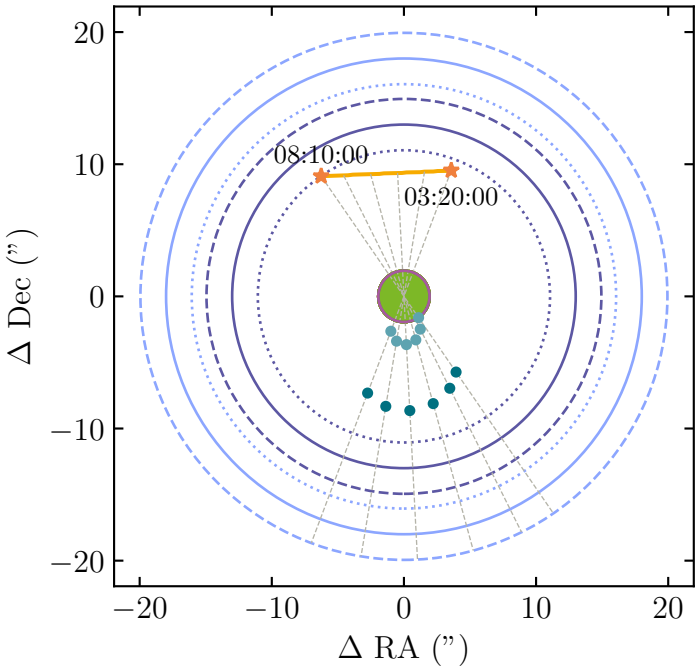

Figure 5.5: Uranus observation window of November 30, 2031 - $m_K < 12$ - $\Delta t = 10$ min - `JPL Horizons` ephemerides.

Table 5.2: Number of observation windows of at least 30 min for Hygiea and Vesta in different configurations - $\Delta t = 5$ min - `JPL Horizons` ephemerides.

Region of interest	Maximum separation to guide star	Hygiea			Vesta		
		$m_{\mathrm{K,\,min}}$			$m_{\mathrm{K,\,min}}$		
		12	13	14	12	13	14
Target limb	18"	82	153	252	22	46	85
	13"	41	78	144	7	8	12
Target center	18"	82	153	78	22	46	84
	13"	41	78	143	7	8	10
Entire target	18"	82	152	248	22	44	80
	13"	39	75	137	7	7	9

number of windows displayed in Table 5.2 for Vesta, an inner main-belt asteroid as well as by the duration of these windows represented in Figure 5.7. Besides, in this case, the number of windows in which the guide star is within 13" from the target is very low, mainly because of the high apparent velocity of this asteroid.

However, contrary to Mars, Hygiea and other main-belt asteroids have a small angular size which enables to observe them entirely during most of the observations as shown by the number of windows where the whole target is observable in Table 5.2.

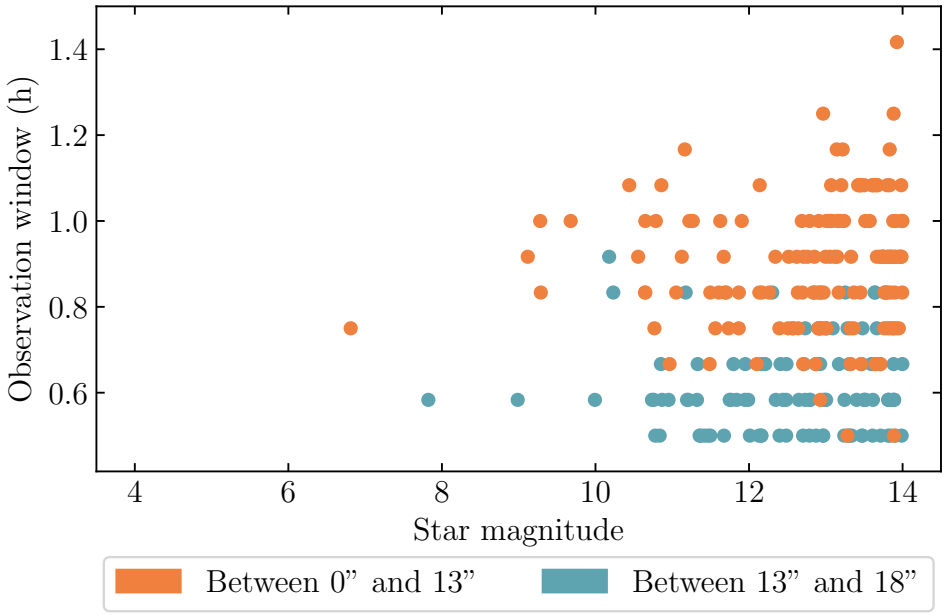

Figure 5.6: Scatter plot of observation window duration as a function of guide star magnitude for windows in which at least a part of the limb of Hygiea is observable - $\Delta t = 5$ min - `JPL Horizons` ephemerides.

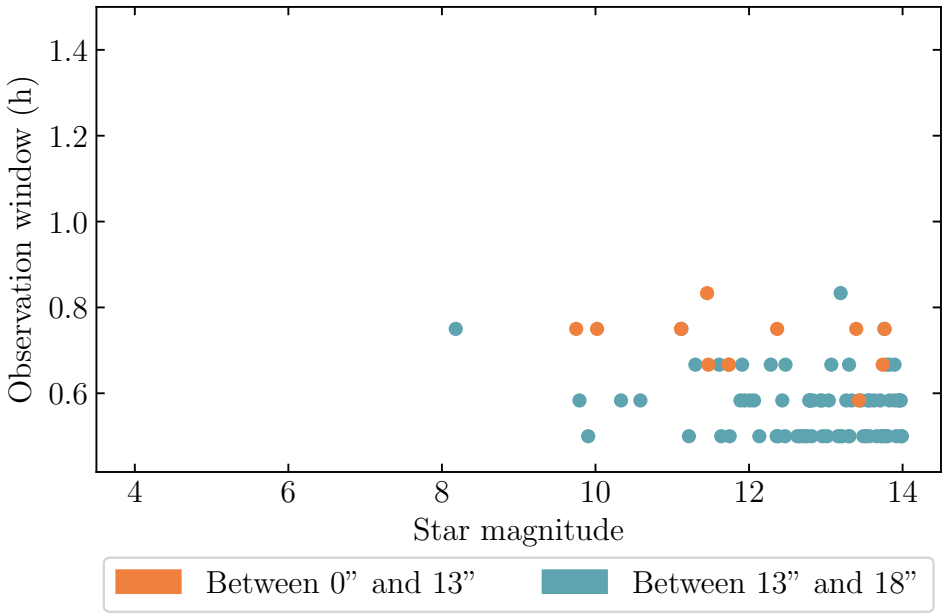

Figure 5.7: Scatter plot of observation window duration as a function of guide star magnitude for windows in which at least a part of the limb of Vesta is observable - $\Delta t = 5$ min - `JPL Horizons` ephemerides.

5.3 Trans-Neptunian objects

For Pluto, it can be seen from Figure 5.8 that very long windows are possible thanks to the slow apparent motion of this trans-Neptunian object. However, and as also noticeable in Table 5.3, there are much less windows than for Uranus or Hygiea. This is unexpected

as Pluto is a very far away object which should enable a lot of long observations. However, the slow orbital motion of Pluto also means that if it is located in a region of the sky where there are few suitable guide stars, it will remain there for a long time. This probably explains the very low number of observation windows for this particular object during the six studied years.

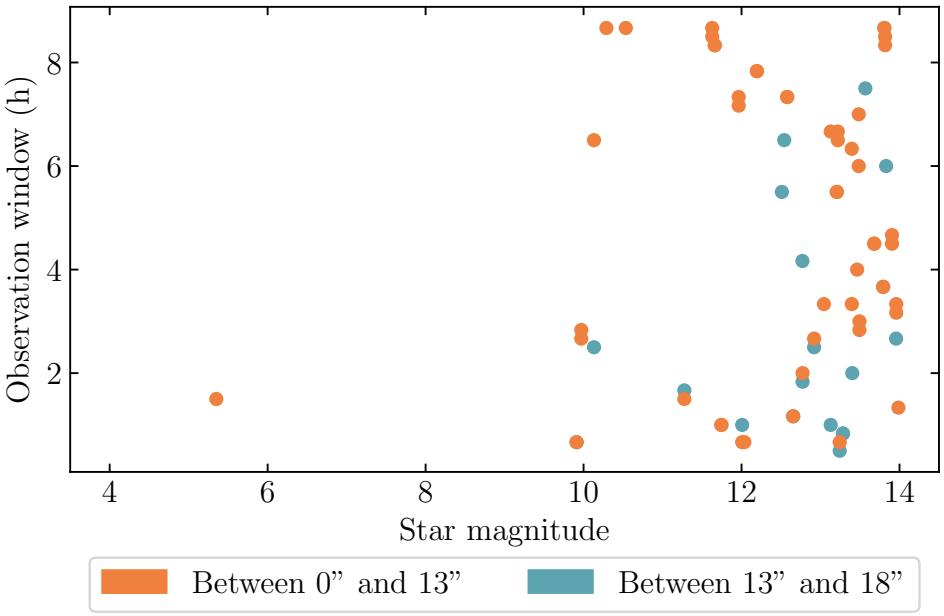

Figure 5.8: Scatter plot of observation window duration as a function of guide star magnitude for windows in which at least a part of the limb of Pluto is observable - $\Delta t = 10$ min - `JPL Horizons` ephemerides.

Table 5.3: Number of observation windows of at least 30 min for Pluto in different configurations - $\Delta t = 10$ min - `JPL Horizons` ephemerides.

Region of interest	Maximum separation to guide star	$m_{\mathrm{K,\,min}}$		
		12	13	14
Target limb	18"	22	36	71
	13"	16	25	50
Target center	18"	22	36	70
	13"	16	24	49
Entire target	18"	22	36	70
	13"	16	24	48

The observation of trans-Neptunian objects will therefore be mainly constrained by their position in the sky. Indeed, while their slow apparent motion allows for very long observation windows, the availability of such windows strongly depends on the stellar density in their background field. If the studied TNO is located in a region with few stars of suitable brightness, there will not be many observation possibilities over an extended

period. On the other hand if the TNO lies in a dense stellar field, it will also remain in that region for a long time, thus enabling a lot of observation windows throughout that period.

Additionally, as for observations of Uranus, the object elevation as well as the one of the Sun will limit the duration of observations of trans-Neptunian objects. Indeed, for many of the short observation windows of Pluto, the guide star is still close to the target at the end of the window or before its beginning therefore meaning that the durations of these windows were driven by the position of the object or the Sun with respect of the observer rather than by the position of the guide star with respect to the object.

Finally, although Pluto has a non-negligible radius, its large distance from the Earth results in a small apparent angular size. As a result, almost all the guide stars associated with the observation windows listed in Table 5.3 enable to observe the entire target.

5.4 Comets

For the three studied comets, as shown in Table 5.4, the number of possible windows varies with the target. However, as the nucleus, which is the most interesting part of comets for mid-infrared observations, is very small for all these targets, the number of windows is the same whether the entire target or only its limb has to be within 18" or 13" from the guide star. Note that the object size considered was the nucleus size since the size of the coma was unknown and vary with the heliocentric distance.

Table 5.4: Number of observation windows of at least 30 min for the three comets - Δt = 5 min for C/2024 E1 and 67P and Δt = 10 min for C/2014 UN271 - `JPL Horizons` ephemerides.

Comet	Maximum separation to guide star	$m_{\mathrm{K,\ min}}$		
		12	13	14
67P	18"	248	349	470
	13"	192	268	358
C/2024 E1	18"	0	0	0
	13"	0	0	0
C/2024 E1 (minimum elevation = 0°)	18"	10	21	60
	13"	5	10	34
C/2014 UN271	18"	27	48	112
	13"	16	29	67

Concerning 67P, there are a lot of windows and, as shown in Figure 5.9, these windows can last for several hours.

However, as visible from Table 5.5, it appeared that these long windows correspond to dates where the comet is not close to its perihelion. Indeed, the farther away the comet

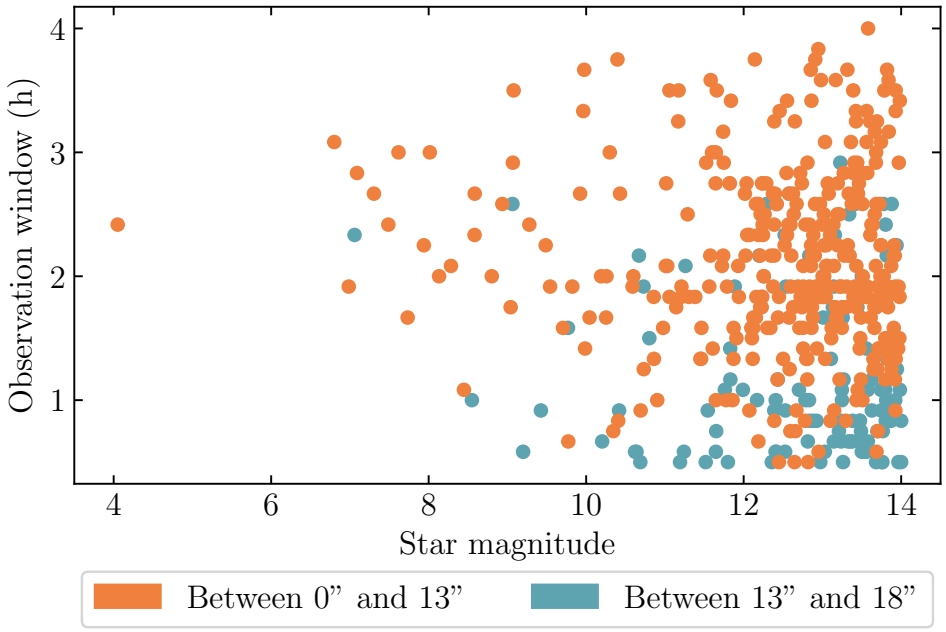

Figure 5.9: Scatter plot of observation window duration as a function of guide star magnitude for windows in which at least a part of the limb of 67P is observable - $\Delta t = 5$ min - `JPL Horizons` ephemerides.

is from the Sun, the lower its orbital velocity and therefore, its apparent motion. Such low apparent motion also enables a higher number of observation windows, as even a star close to the edge of the region where guide stars can be located may remain within that region for at least 30 min if the target moves slowly enough.

Table 5.5: Number and maximum duration of observation windows of 67P for different maximum heliocentric distances - $m_K < 14$ - $\Delta t = 5$ min - `JPL Horizons` ephemerides.

Maximum heliocentric distance (AU)	Maximum separation to guide star		Maximum window duration
	13”	18”	
1.5	0	0	-
2.5	1	8	55 min
3.5	2	9	55 min
4.5	160	194	2 h 40 min
5.5	325	406	3 h 50 min
6.5	354	470	4 h 00 min

Yet, comets are usually observed when they are close to the Sun, typically at less than 1.5 AU. As shown in Table 5.5, below such a distance there is no window enabling to observe the comet for at least 30 min. The first window of at least 30 min occurs on July 10, 2034 when the comet is at 1.83 AU.

The constraint on the duration of the observation window was thus relaxed to determine if an observation was possible below 1.83 AU. It appeared that a few windows of more than 25 min are then still possible until the 22 min window of August 8, 2034 when the comet is at 1.63 AU. As visible in Figure 5.10, the duration of these windows is limited by the comet velocity. Since this velocity is even higher when the comet is at an heliocentric distance of less than 1.5 AU, this explains why there is no observation windows enabling to observe 67P when it is the most active.

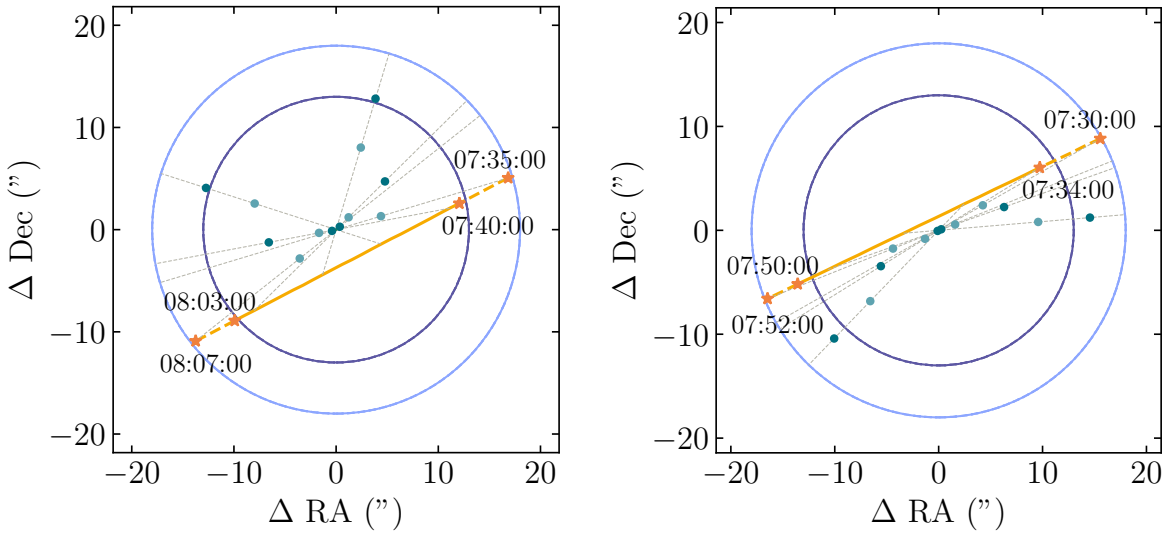

(a) July 10, 2034 - $d_{\text{Sun}} = 1.83$ AU.

(b) August 8, 2034 - $d_{\text{Sun}} = 1.63$ AU.

Figure 5.10: Observations windows of 67P when the comet is closer than 2 AU from the Sun - $m_K < 14$ - $\Delta t = 1$ min - `JPL Horizons` ephemerides.

For C/2024 E1, no observation window of 30 min was identified during the six studied years. However, this is mainly due to the low elevation of this target. Indeed, considering an unrealistic minimum elevation of 0° would enable to find several windows that, as shown in Figure 5.11, could last for several hours. Nevertheless, none of these windows occurs when the comet is close to the Sun than 1.5 AU. Indeed, the first window of 30 min occurs when the comet is at 2.2 AU from the Sun.

For C/2014 UN271, there are far fewer windows but as noticeable in Figure 5.12, these windows can last for several hours. Once again, the most interesting observation windows correspond to times when the comet is near its perihelion. However, this comet has a very far perihelion of 10.97 AU and it will thus be much slower than 67P. This perihelion is scheduled to be reached around January 21, 2031 after which the comet will slowly move away from the Sun [26]. A few observation windows are possible around this date and, in particular, a 4 h 30 min window of January 22 represented in Figure 5.13. This figure also highlights the fact that, as for other far away objects such as Pluto, the duration of the observation windows will be mainly constrained by the elevation of the target and the Sun as the differential motion between the object and the guide star will be very slow.

Finally, concerning the low number of possible observations of this comet, it can be explained by its high inclination that probably results in the crossing of a region far less

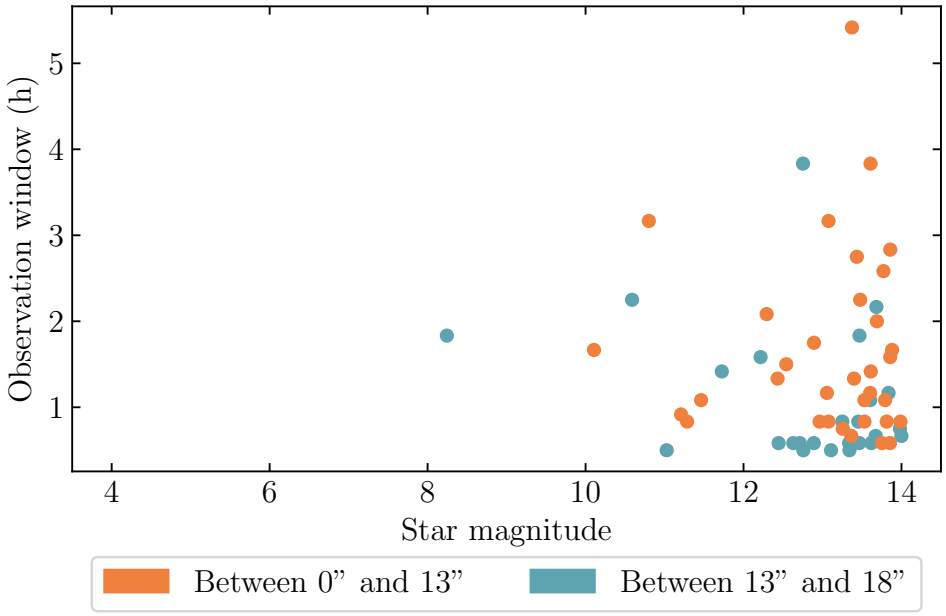

Figure 5.11: Scatter plot of observation window duration as a function of guide star magnitude for windows in which at least a part of the limb of C/2024 E1 is observable with a minimum elevation of 0° - $\Delta t = 5$ min - `JPL Horizons` ephemerides.

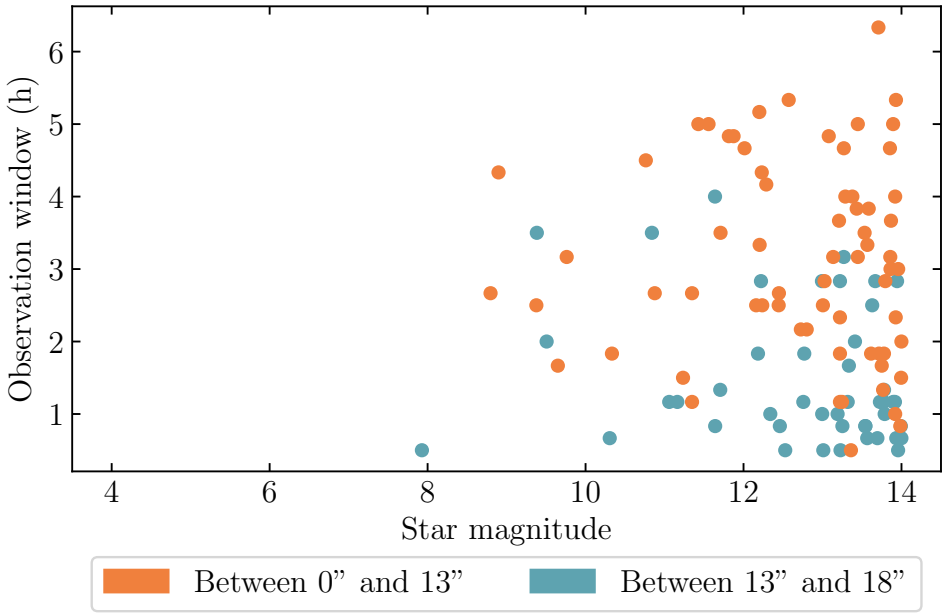

Figure 5.12: Scatter plot of observation window duration as a function of guide star magnitude for windows in which at least a part of the limb of C/2014 UN271 is observable - $\Delta t = 10$ min - `JPL Horizons` ephemerides.

densely populated with stars than the galactic plane.

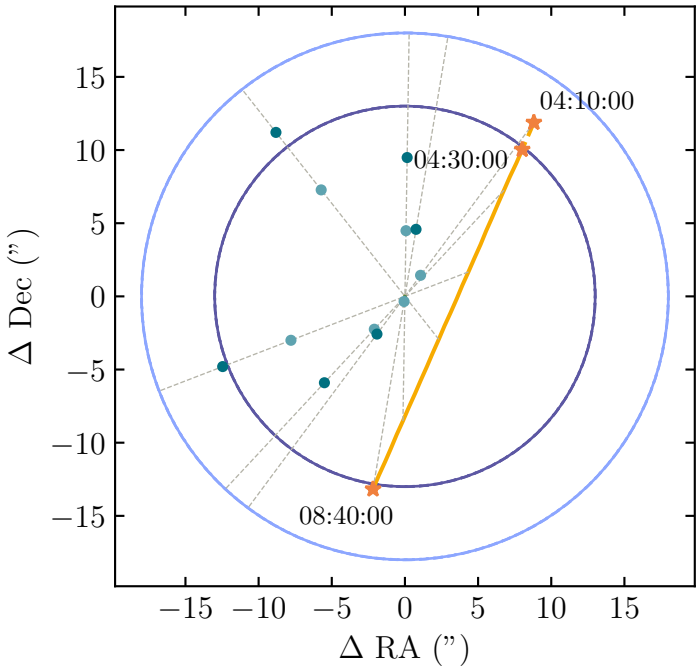

Figure 5.13: Observation window of C/2014 UN271 on January 22, 2031 - $m_K < 12$ - $\Delta t = 10$ min - `JPL Horizons` ephemerides.

5.5 Moons

For Io, as shown in Table 5.6, two different constraints on the distance between Jupiter's limb and the one of its moon have been studied. First, a minimum distance of 13.5" between the two has been imposed in order to ensure that Jupiter will always be outside the imager during the observations. Since such separation could still lead to some stray light effect, a minimum distance of 27" also has been considered.

Table 5.6: Number of observation windows of at least 30 min for Io in different configurations - $\Delta t = 10$ min - `Astropy` and `JPL Horizons` ephemerides.

Region of interest	Maximum separation to guide star	$d_{\text{Io - Jupiter}} = 13.5$"			$d_{\text{Io - Jupiter}} = 27$"		
		$m_{\text{K, min}}$			$m_{\text{K, min}}$		
		12	13	14	12	13	14
Target limb	18"	217	294	410	196	263	368
	13"	153	231	314	135	205	283
Target center	18"	216	294	404	192	261	360
	13"	141	220	300	125	199	271
Entire target	18"	209	282	390	187	254	350
	13"	131	206	287	119	190	261

In both cases, there is a high number of possible observation windows and as shown

in Figure 5.14, these windows can last for several hours. However, some windows are slightly reduced when considering a minimum separation of 27" compared to the case with a separation of at least 13.5". This is especially the case for the longest windows which are reduced by approximately 30 min.

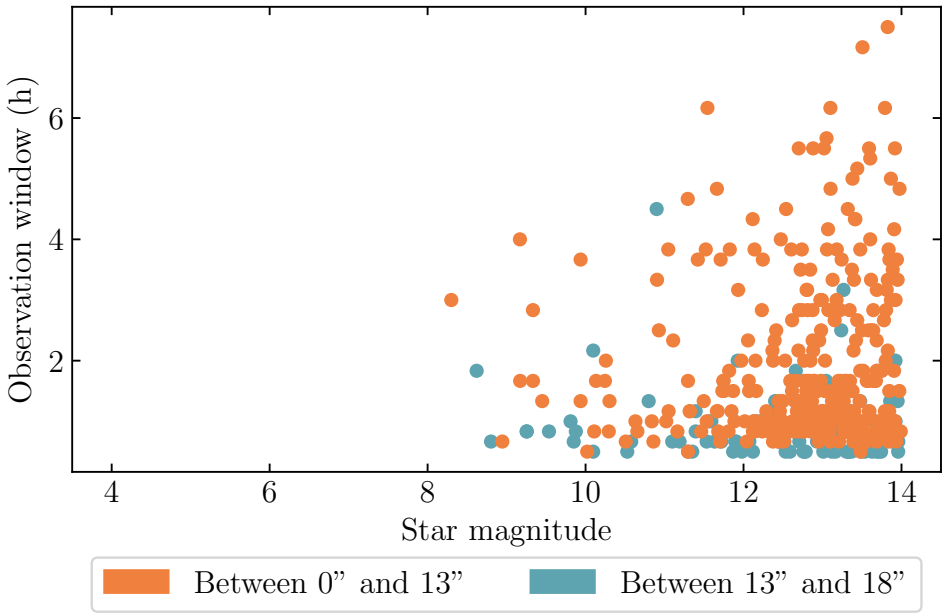

(a) $d_{\text{Io - Jupiter}} = 13.5"$.

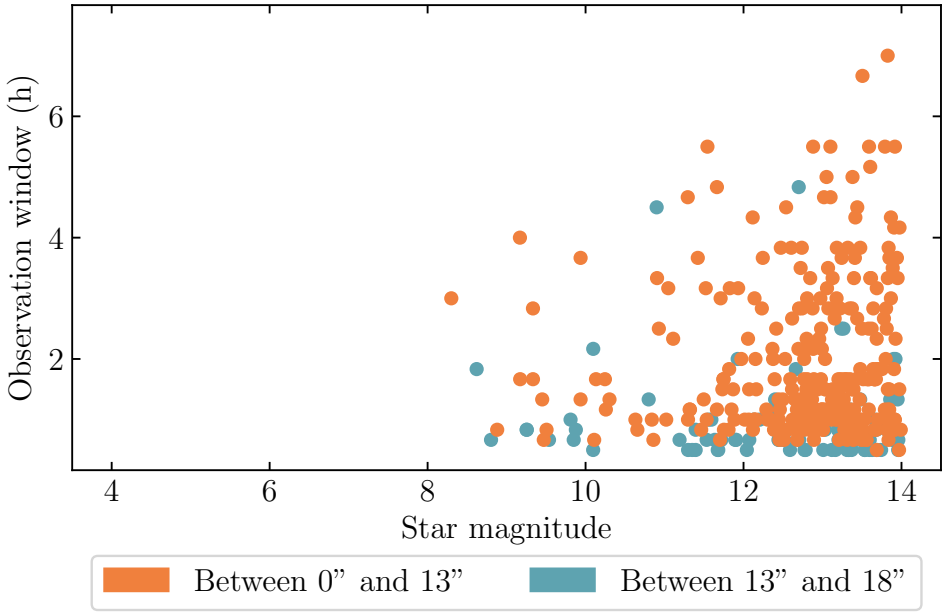

(b) $d_{\text{Io - Jupiter}} = 27.0"$.

Figure 5.14: Scatter plot of observation window duration as a function of guide star magnitude for windows in which at least a part of the limb of Io is observable - $\Delta t = 10$ min - `JPL Horizons` ephemerides.

Note also that, as represented in Figure 5.15, the duration of the observation windows will mainly be constrained by the position of the moon on its orbit around the planet.

Indeed, as visible in these figures, a similar angular distance can be covered by the moon over very different amounts of time. If Io is at its largest apparent angular separation from Jupiter, the window is longer because the moon is actually moving towards or away from the Earth. On the other hand, when its motion is transverse to the line of sight, it appears to move faster in the sky.

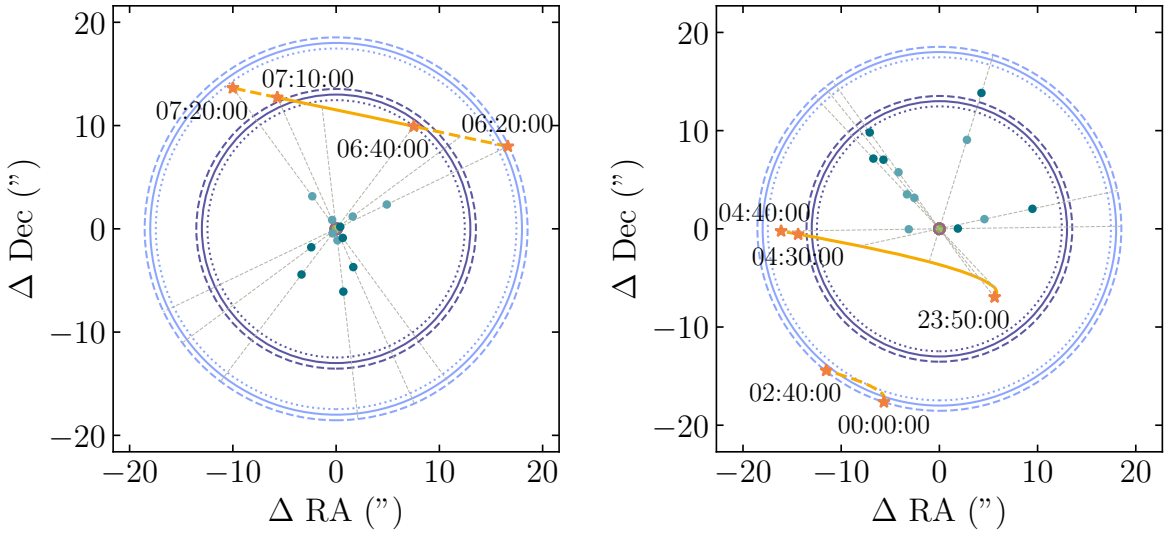

(a) April 1, 2030.

(b) August 15, 2031.

Figure 5.15: Io observation windows - $d_{\text{Io - Jupiter}} = 13.5$" - $m_K < 12$ - $\Delta t = 10$ min - `JPL Horizons` ephemerides.

5.6 Jupiter's aurorae

Concerning Jupiter's aurorae, given the values of Figure 5.16, if the target is the north pole aurora, the Jupiter System III longitude has to be comprised between 110 and 260° whereas it had to be between 0 and 100° for the south pole aurora.

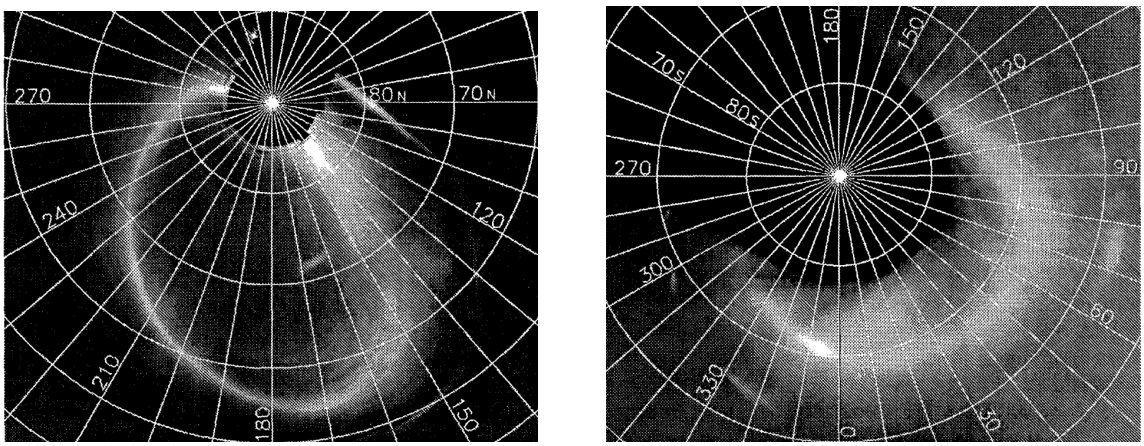

(a) Northern auroral oval.

(b) Southern auroral oval.

Figure 5.16: Projected views of Jupiter's north and south polar regions. Grid lines indicate System III longitude and planetocentric latitude lines [27].

Moreover, only stars enabling to observe Jupiter between 45 and 90° of latitude north or south are retained as it corresponds to the zone in which aurorae are located. This leads to the non-circular regions where stars can be located represented in Figure 5.17.

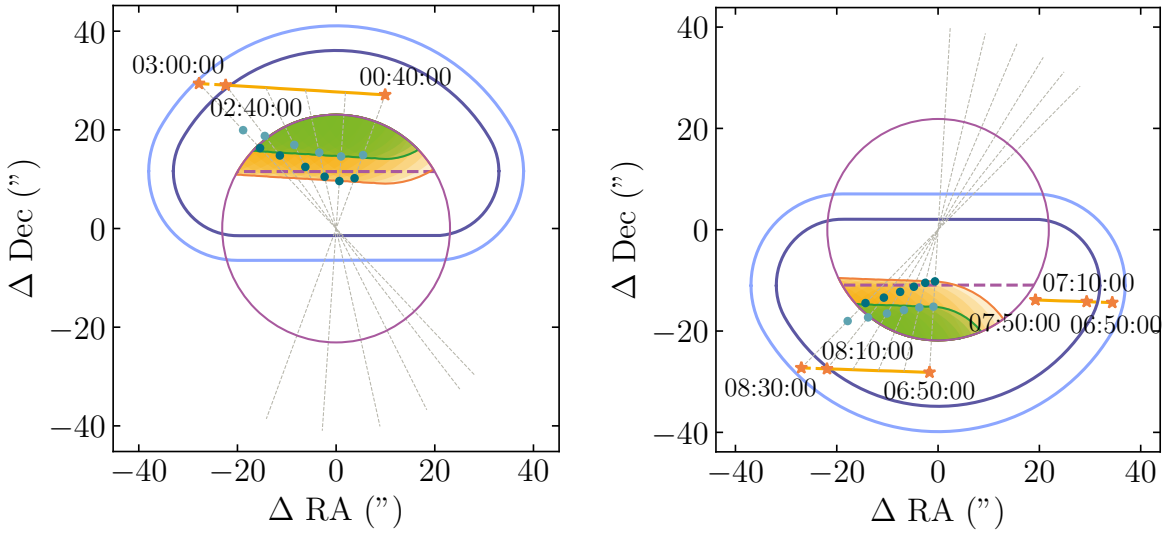

(a) Norther-auroral oval - June 11, 3031.

(b) Southern auroral oval - May 6, 2031.

Figure 5.17: Jupiter aurorae observation windows - $m_K < 12$ - $\Delta t = 10$ min - `JPL Horizons` ephemerides.

As shown in Table 5.7, several windows meet these criterion though all of them only enable to observe a part of the aurora because of the large angular size of Jupiter. It also appears that there are more windows enabling to observe the northern aurora than the southern one. This is due to the fact that the range of acceptable longitudes in Jupiter System III is larger for the northern auroral oval (150°) than for the southern one (100°). This extended range of longitude for the northern aurora also leads to longer observation windows than for the southern aurora as represented in Figure 5.18.

Table 5.7: Number of observation windows of at least 30 min for Jupiter's aurorae in different configurations - $\Delta t = 10$ min - `JPL Horizons` ephemerides.

Region of interest	Maximum separation to guide star	$m_{\mathrm{K,\ min}}$		
		12	13	14
North pole	18"	183	249	319
	13"	141	189	237
South pole	18"	135	190	242
	13"	107	150	194

Furthermore, the duration of the observation windows appears to be mainly determined by the allowed longitude ranges for each pole. Indeed, for the northern aurora, windows can last up to around 4 h which, since Jupiter System III has a rotation period of 9.92 h, corresponds to the amount of time necessary to go from 110° of longitude

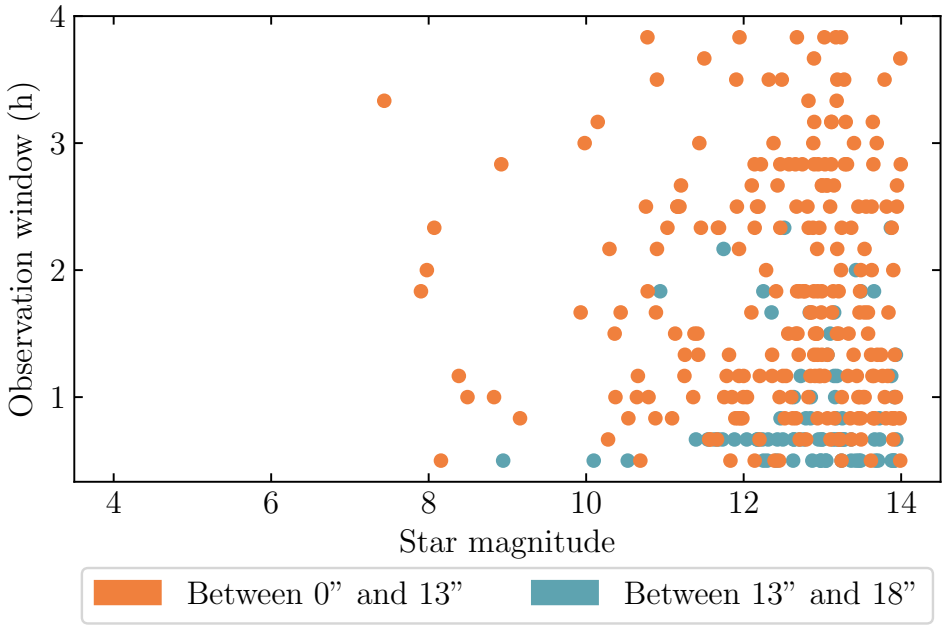

(a) Northern auroral oval.

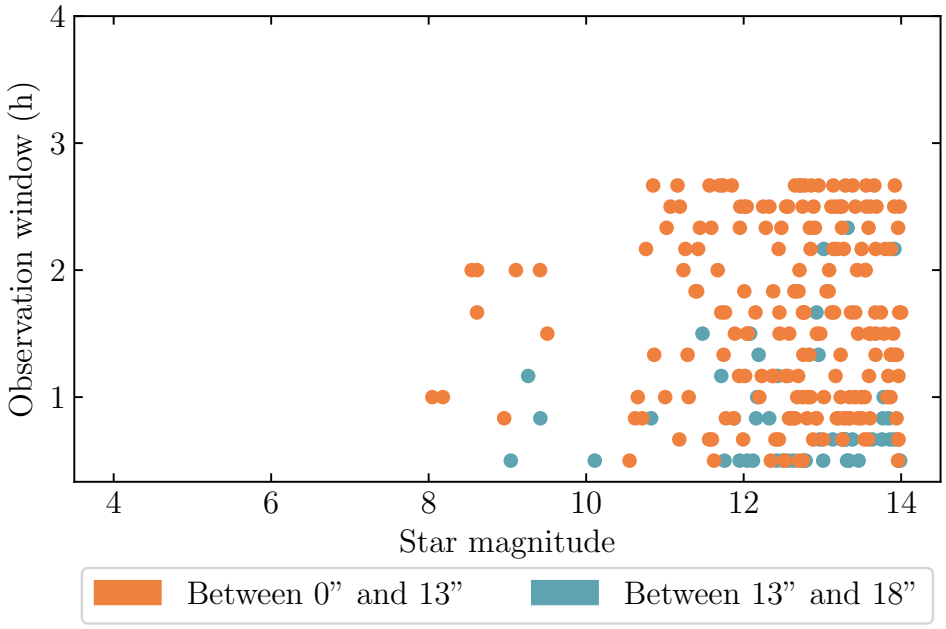

(b) Southern auroral oval.

Figure 5.18: Scatter plot of observation window duration as a function of guide star magnitude for observations of a part of Jupiter's auroral ovals - $\Delta t = 10$ min - `JPL Horizons` ephemerides.

to 260°. On the other hand, 2 h 45 min are required to rotate from 0° to 100° which approximately corresponds to the longest windows possible for the southern aurora.

Note however that, as illustrated in Figure 5.19, some windows only enable to observe a small fraction of the zone of interest. A constraint that the whole area must be observable during at least 30 min was tested, but given Jupiter's angular size and the position of the

region of interest, this proved impossible. Nevertheless many windows enable to observe a significant fraction of Jupiter, especially if they last for several hours.

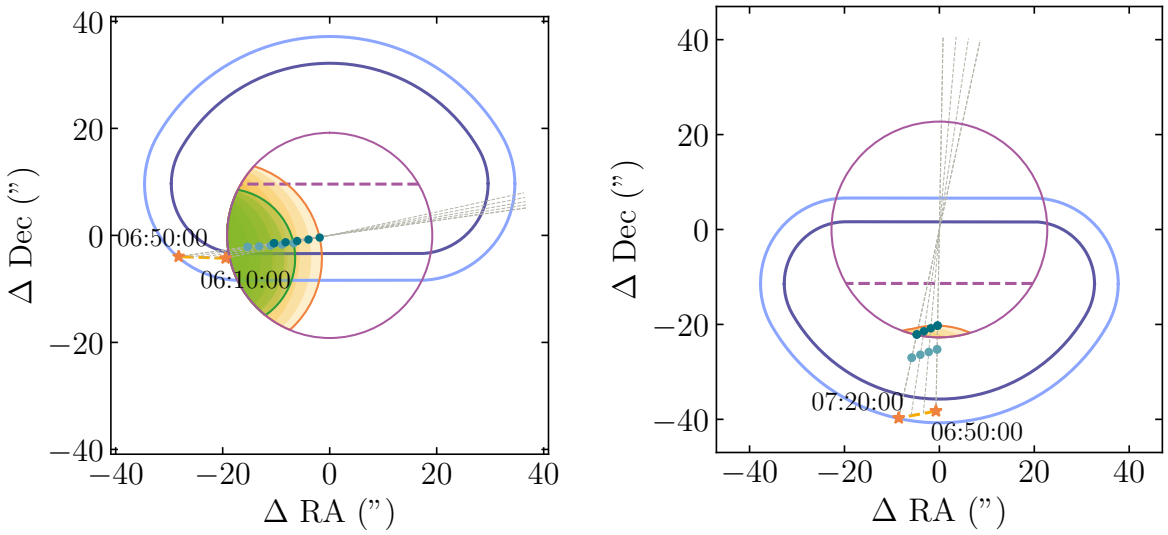

(a) Norther-auroral oval - March 23, 3031.

(b) Southern auroral oval - June 11, 2033.

Figure 5.19: Jupiter aurorae observation windows only enabling to observe a small fraction of the aurora - $m_K < 12$ - $\Delta t = 10$ min - `JPL Horizons` ephemerides.

5.7 Discussion

5.7.1 Influence of guide star magnitude

From the results of the different test cases, it can be seen that when considering the conservative case where the guide star must be brighter than magnitude 12, there is already a substantial number of windows for many targets. Indeed, there is on average at least 1 window per month with a star within 18” from the object limb for all targets except Mars, Pluto, Vesta and C/2014 UN271. For Pluto and C/2014 UN271, the lower number of windows is explained by a slow object moving in a field with few stars. On the other hand, for Mars and Vesta, this low number of windows is caused by the high apparent motion of these objects.

Extending the acceptable magnitude range to its theoretical limit of 14 enables to increase the number of possible windows by a factor 1.7 to 4.1 depending on the object and the region of interest considered. If this limit turns out in practice to be lower than expected, using only star brighter than magnitude 13 still enables to increase the number of windows by a factor 1.3 to 2.1 with respect to the case with stars brighter than magnitude 12. It also appears that, for most cases where the increase factor between the number of windows with a guide star brighter than magnitude 12 and the cases with a star brighter than magnitude 14 is below 2, the target is a target where additional constraints where added, *i.e.*, Jupiter’s aurorae or Io. The only other target that is associated to an increase factor lower than 2 is 67P. On the other hand, the ratios remains similar for a given target whatever the region of interest considered.

5.7.2 Influence of angular separation between target and guide star

Concerning the two separations between guide star and target considered, the 18" separation logically enables to obtain more observation windows for all targets. In general, increasing the separation from 13" to 18" indeed increases the number of windows by a factor 1.3 to 2.2 except for Vesta where the increase factor can reach 7.1 because of the very low number of windows for which the guide star remains at least 30 min within 13" from this asteroid. For most cases, this factor seems to slightly decrease when going to a less restrictive constraint on the star magnitude probably because of the higher number of stars that can then be used as guide stars. Moreover, for the case of targets of large angular radius such as Uranus or Io, the increase factor is larger if the whole target has to be within 13" or 18" from the guide star than if the separation is considered between the object limb and the star. This is easily explained by the fact that the target size will reduce the zone in which guide stars can be located. For example, for Uranus and stars brighter than magnitude 12, if the region of interest is the planet limb, going from a search zone radius of 13" to a radius of 18" leads to an increase of the number of windows by a factor 1.7 while, if the region of interest is the entire target, the increase factor is equal to 2.2.

5.7.3 Influence of target configuration

Concerning the three studied configurations of the target, the evolution of the number of possible windows when going from the less restrictive case where only a part of the target limb must be within 13" or 18" from the guide star to the case where all the target must lie whithin 13" or 18" during the whole observation window is strongly dependent on the target angular size.

In the case of targets of very small angular size such as Hygiea, Vesta or Pluto, considering that the star has to be within 13" or 18" from the target limb, its center or the entire target does not lead to a large difference in the number of possible windows. Indeed, whatever the requirement on the guide star magnitude, the number of windows only decreases by a few percents when comparing the results of the case where at least a part of the object must be within 13" or 18" from the star to those of the case where the entire object is separated by maximum 13" or 18" from the star.

On the other hand, for Io, as this target has a larger angular size, the decrease in number of windows is larger and can reach 15 % in the case of stars brighter than magnitude 12 and a maximum separation of 13" between the guide star and the target. This effect is even more noticeable for Uranus, where the number of windows can be reduced by up to 46 % by considering that the entire target has to be within 13" or 18" from the guide star compared to the case where this distance is to be measured from the target limb.

This phenomenon can once again be explained by the fact that a larger angular size will greatly reduce the region in which the guide star can be located if the entire target

has to be within 13" or 18" from the star. Indeed, the radius of this region is then equal to 13" or 18" minus the target angular radius whereas it would be of 13" or 18" plus the target angular radius in the case where the only requirement is to observe at least a part of the target limb.

Finally, note that imposing a minimum distance of 1" between the target limb and the guide star does not lead to a significant decrease of the number of windows. Indeed, for the different test cases, if this requirement was removed, less than 10 additional windows are found in the most extreme cases.

CHAPTER 6

ON-AXIS GUIDING ON SCIENCE TARGETS

As shown in the previous chapter, the number of windows can be pretty low for some objects such as main-belt asteroids or trans-neptunian objects. Additionally, for main-belt asteroids, these windows are always shorter than 2 hours. However, if these targets could be used as "guide star" in the AO system, the number and duration of windows would in principle be only limited by the visibility of the target from the observatory, and potentially its position on its orbit. This chapter thus focuses on determining if some asteroids or TNOs could be used in the AO system.

The main constraints for a target to be used as "guide star" are first described before studying separately the cases of the asteroids and the TNOs.

6.1 Constraints

Since the maximum modulation radius of the pyramid wavefront sensor is equal to $10\lambda/D$, the theoretical maximum angular diameter for a target to be used as "guide star" in the AO system is equal to $10\lambda/D = 0.109$" by considering $\lambda = 2.0$ μm, the lower boundary and most restrictive wavelength of the K-band. Such angular diameter will ensure that the entire object will pass from one quadrant of the pyramid to the other. Larger objects could still be considered but their apparent magnitude as perceived by the pyramid would be reduced because some regions of the object would always remain in the same region of the pyramid. This possibility is already studied by the METIS SCAO team at Heidelberg but the results of the study are not yet available. Besides, the more extended the object is, the less sensitive the sensor becomes to aberrations thus leading to a decrease of the correction performance.

Depending on the object-Sun distance and on the phase angle, this maximum angular diameter will translate into different maximum object diameters. On the other hand, the minimum diameter will be constrained by the target apparent magnitude in K-band. Indeed, for point-like sources, the METIS AO system is expected to operate on targets brighter than magnitude 14 in the K-band, and for extended sources, a stricter bright-

ness requirement is likely, as their flux is spread over a larger area. Since the apparent magnitude of a given target depends on its size, spectral type, and its distances to both the Sun and the observer, this translates in a requirement on the minimum diameter.

6.2 Asteroids

6.2.1 Asteroid magnitude

The apparent magnitudes of asteroids vary as a function of their phase angle, *i.e.*, the angle formed by the Sun, the asteroid and the observer, and exhibit a brightness increase when close to the opposition. This dependence on the phase angle can be modeled through two magnitude systems: the HG-system or the HG_1G_2 system where H refers to the absolute magnitude of the asteroid and G, G_1, G_2 refers to coefficients modeling the dependence of the apparent magnitude on the phase angle.

In the HG-system, the apparent magnitude of an asteroid, m, is given by:

$$m = H + 5\ \log_{10}(d_{\mathrm{AS}} d_{\mathrm{AO}}) - 2.5\ \log_{10} q(\alpha), \tag{6.1}$$

where d_{AS} is the distance between the asteroid and the Sun, d_{AO}, the distance between the asteroid and the observatory, both of them being expressed in astronomical units, H is the asteroid absolute magnitude and $q(\alpha)$ is the phase integral [28]. This phase integral expresses the magnitude variation as a function of the phase angle α and is equal to:

$$q(\alpha) = (1 - G)\phi_1(\alpha) + G\phi_2(\alpha) \tag{6.2}$$

with

$$\phi_1(\alpha) = \exp\left(-3.332\left(\tan\frac{\alpha}{2}\right)^{0.631}\right), \tag{6.3}$$

$$\phi_2(\alpha) = \exp\left(-1.862\left(\tan\frac{\alpha}{2}\right)^{1.218}\right), \tag{6.4}$$

the phase functions describing the magnitude variation as a function of the phase angle. In Equation 6.2, the slope parameter G describes the increase in brightness that occurs when the asteroid is near opposition. Since its value is accurately known for only a few asteroids, a value of $G = 0.15$ is often assumed to characterize magnitude variations in the V-band [29]. Note also that the above relations are valid if the phase angle is smaller than 120° and works best when $\alpha < 20^\circ$.

The HG_1G_2 system is an improved version of the HG-system in which the phase integral is given by:

$$q(\alpha) = (1 - G_1 - G_2)\phi_0(\alpha) + G_1\phi_1(\alpha) + G_2\phi_2(\alpha), \tag{6.5}$$

where values of $\phi_0(\alpha)$, $\phi_1(\alpha)$ and $\phi_2(\alpha)$ can be interpolated from tabulated values through a cubic spline [30]. Concerning G_1 and G_2, typical values of these parameters have been estimated for different asteroid classes and are given in Table 6.1.

Table 6.1: Average G_1 and G_2 parameters for main asteroid classes [30].

Asteroid type	G_1	G_2
S	$0.26^{+0.01}_{-0.01}$	$0.38^{+0.01}_{-0.01}$
M	$0.27^{+0.03}_{-0.02}$	$0.35^{+0.01}_{-0.01}$
E	$0.15^{+0.02}_{-0.02}$	$0.60^{+0.01}_{-0.01}$
C	$0.82^{+0.02}_{-0.02}$	$0.02^{+0.02}_{-0.01}$
D	$0.96^{+0.02}_{-0.03}$	$0.02^{+0.02}_{-0.02}$
All types	$0.55^{+0.06}_{-0.06}$	$0.24^{+0.04}_{-0.04}$

In both systems, the asteroid absolute magnitude in V-band can be computed based on its diameter, D and geometric albedo in the V-band p_V through [31]:

$$H = 5 \ \log_{10}\left(\frac{1329}{D\sqrt{p_V}}\right). \tag{6.6}$$

The value of p_V to be used in the above formula is different depending on the asteroid type. As shown in Table 6.2, carbonaceous asteroids such as C-type and D-type asteroids have a very low albedo whereas asteroids rich in enstatite such as E-type asteroids have a very high albedo. Finally, the S-type asteroids, rich in silicates, and the M-type asteroids, rich in metals, have an intermediate albedo.

Table 6.2: Average geometric albedos for main asteroid classes [30].

Asteroid type	Albedo (-)
S	0.22 ± 0.05
M	0.17 ± 0.07
E	0.45 ± 0.07
C	0.061 ± 0.017
D	0.049 ± 0.022

No relation such as Equation 6.6 has been established for magnitudes in K-band and the albedos of asteroids in this band are also poorly known. However, magnitude differences between V and K band can be estimated. This difference can be considered roughly equal to 1.5 for S-type asteroids, $2.0 - 2.5$ for C-type asteroids and $2.5 - 3.5$ for D-type asteroids [32]. These values can be averaged to an approximate difference of 2.5 for all asteroid types [33].

Therefore Equations 6.1 and 6.6 have been used to determine the asteroid magnitude in the V-band. Based on this result, the asteroid apparent magnitude in K-band has been derived through the $V - K$ differences associated to each asteroid type. Note that since there was no value for the M-type and E-type asteroids, the mean value for all asteroids has been used.

6.2.2 Results

The asteroid magnitudes were first computed using the HG magnitude system. Since in this model the only parameter influenced by the asteroid types is their albedo, the average value of $V - K = 2.5$ has been considered for all types. Besides, as shown in Table 6.2, asteroid geometric albedo in V-band can vary between 0 and 0.5 depending on the asteroid type so that different values of this parameter have been considered between the two boundaries. Finally, four asteroid-Sun distances have been studied: 2.10 AU, 2.65 AU, 3.20 AU (inner, middle and outer main-belt) and 5.20 AU (Jupiter Trojans), with a 0° phase angle and the maximum phase angle associated to each of these four distances. Note also that all the studied cases assume a Sun-Earth distance of 1 AU.

As visible in Figures 6.1 to 6.4, for the four studied distance, there is indeed a range of asteroid diameters that should allow the METIS AO system to work. This range varies from a few dozen of kilometers to a few hundreds depending on the considered distance and albedo. As expected, for a given asteroid-Sun distance, the range of acceptable diameters shifts to larger diameters as the phase angle increases. Indeed, an increase in phase angle leads to a larger distance between the Earth and the target and, therefore, a given asteroid becomes fainter and its angular diameter decreases. For example, for an asteroid-Sun distance of 2.65 AU and a phase angle of 0°, asteroids between 4 and 139 km could be used as "guide stars" while they must have diameters between 10 and 218 km at a phase angle of 28°.

The range of diameters is also shifted to larger diameters for increasing values of the distance between the asteroid and the Sun. As visible in Figures 6.1a and 6.4a, for a phase angle of 0°, if the asteroid is located at 2.1 AU from the Sun, it must be between 2 and 93 km in diameter to be used in the AO system whereas, for a distance of 5.2 km, it must be between 21 and 354 km. Once again, this is explained by a higher distance between the observatory and the target.

Moreover, the asteroid albedo also has a high influence on the minimum asteroid diameter leading to an apparent magnitude brighter than magnitude 14. For example, for an asteroid-Sun distance of 2.10 AU and a phase angle of 0°, an albedo of 0.005 would lead to a minimum diameter of 22 km whereas an albedo of 0.5 would enable to use asteroids of diameters up to 2 km.

These values can be refined depending on the main asteroid types found in the main-belt and among Jupiter trojans. As shown in Table 6.3 and Table 6.4, both magnitude systems lead to similar minimum diameters. On the other hand, the different albedo ranges of the various asteroid classes strongly impacts the minimum diameter required to reach magnitude 14. Indeed, asteroids of high albedos such as E-type asteroids can be used as guide objects up to a diameter three times smaller than C-type asteroids which have a very low albedo. However, in the main-belt, E-type asteroids are very rare whereas C-type asteroids approximately represents 75% of the asteroids, S-type asteroids, 17% of asteroids and M-type asteroids, 7%. Concerning Jupiter trojans, most of them are of the D-type and have a very low albedo so that the minimum diameter will be much larger than it could have been by considering albedos ranging up to 0.5.

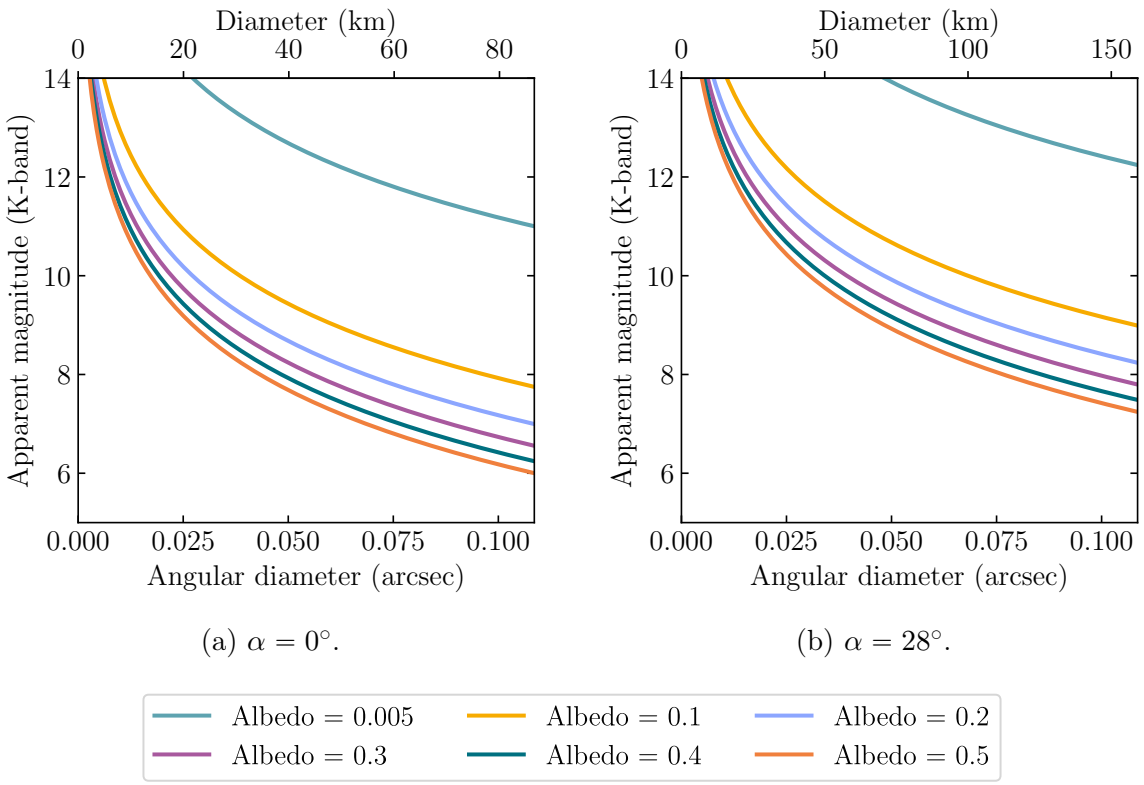

(a) $\alpha = 0°$. (b) $\alpha = 28°$.

Figure 6.1: Variation of asteroid apparent magnitude as a function of their diameter for different albedos - $d_{\mathrm{AS}} = 2.10$ AU - $V - K = 2.5$ mag.

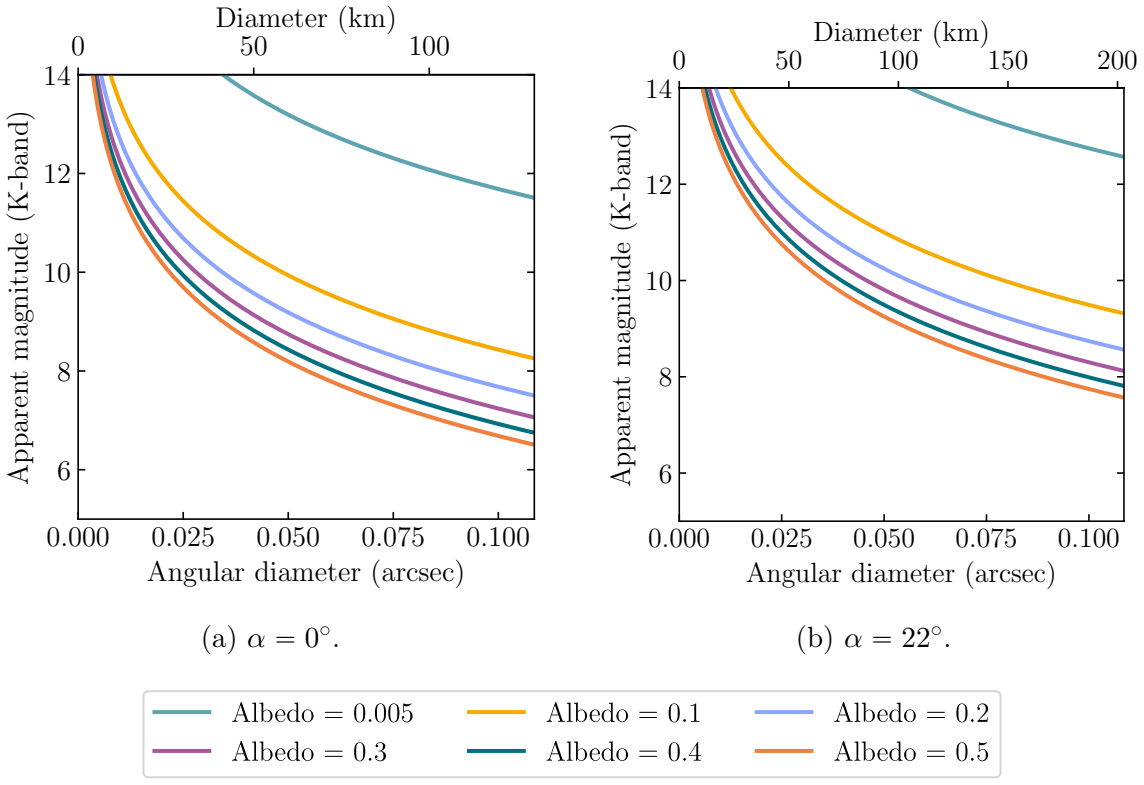

(a) $\alpha = 0°$. (b) $\alpha = 22°$.

Figure 6.2: Variation of asteroid apparent magnitude as a function of their diameter for different albedos - $d_{\mathrm{AS}} = 2.65$ AU - $V - K = 2.5$ mag.

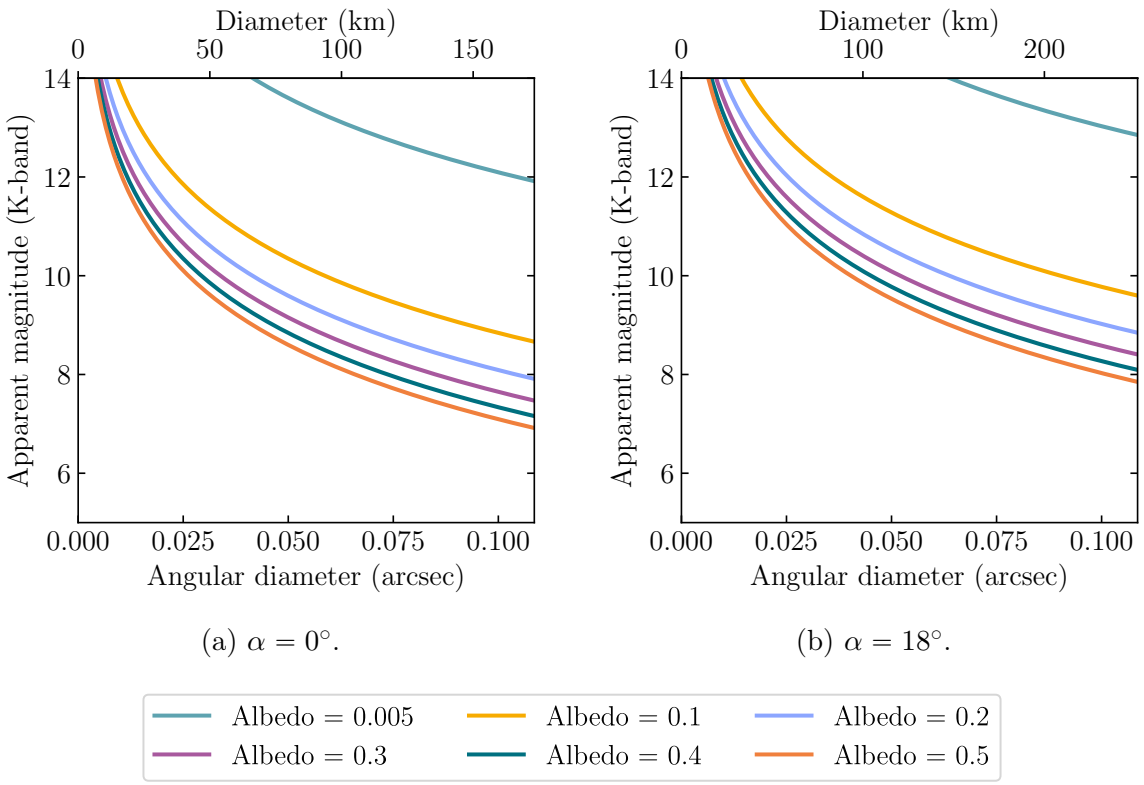

(a) $\alpha = 0°$. (b) $\alpha = 18°$.

Figure 6.3: Variation of asteroid apparent magnitude as a function of their diameter for different albedos - $d_{AS} = 3.20$ AU - $V - K = 2.5$ mag.

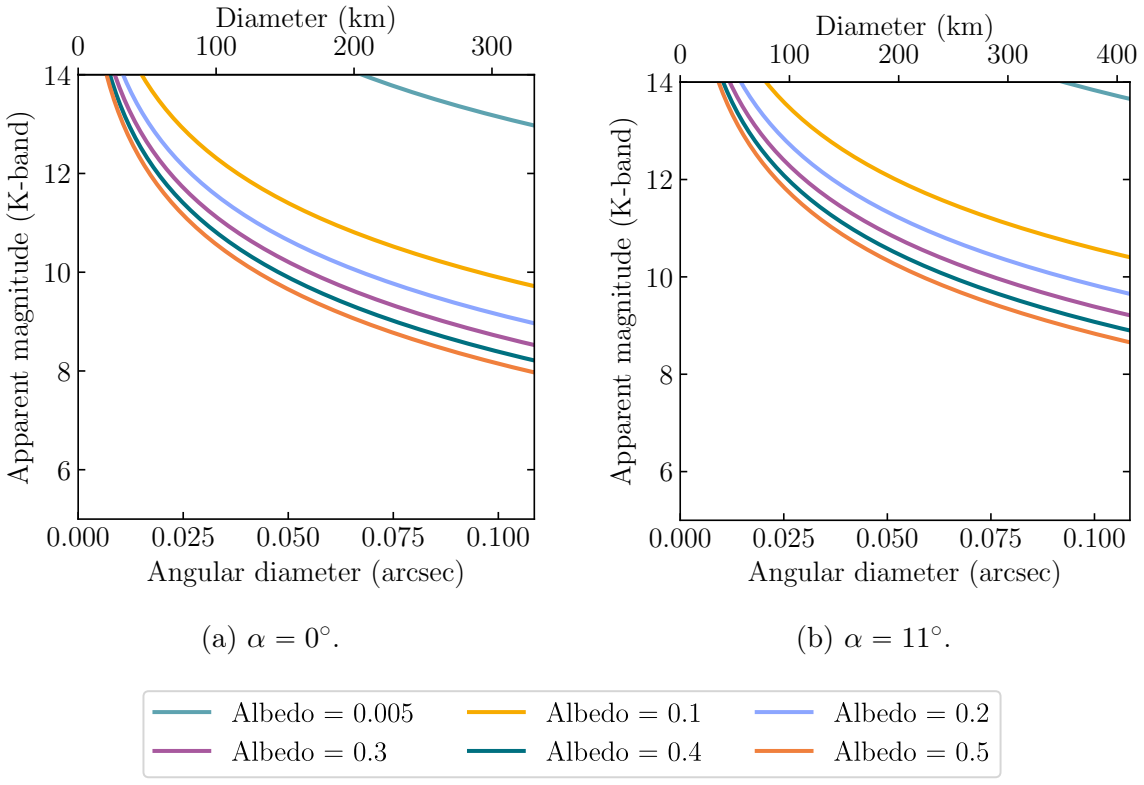

(a) $\alpha = 0°$. (b) $\alpha = 11°$.

Figure 6.4: Variation of asteroid apparent magnitude as a function of their diameter for different albedos - $d_{AS} = 5.20$ AU - $V - K = 2.5$ mag.

Table 6.3: Minimum and maximum diameter enabling main-belt asteroids to be used in the AO system with $m_K < 14$ for various asteroid-Sun distance and minimum and maximum phase angles. HG indicates values computed with the HG magnitude system and HG_1G_2 those obtained with the HG_1G_2 magnitude system. S, C, M and E respectively correspond to diameters obtained with albedos and $V-K$ values, as well as G_1 and G_2 values when relevant, associated to S-type, C-type, M-type and E-type asteroids (using $V-K=2.5$ in this latter case). For the maximum diameter, no distinction is made between the different asteroid types as it is only defined by the maximum angular diameter of 0.109" and the distance between the asteroid and the observer.

d_{AS} (AU)	2.10 ($\alpha = 0°$)	2.10 ($\alpha = 28°$)	2.65 ($\alpha = 0°$)	2.65 ($\alpha = 22°$)	3.20 ($\alpha = 0°$)	3.20 ($\alpha = 18°$)
d_{max} (km)	87	159	130	203	173	251
$d_{\mathrm{min},HG,C}$ (km)	6	20	12	30	19	42
$d_{\mathrm{min},HG,S}$ (km)	5	15	9	23	14	32
$d_{\mathrm{min},HG,M}$ (km)	3	10	6	15	10	21
$d_{\mathrm{min},HG,E}$ (km)	2	7	4	10	7	15
$d_{\mathrm{min},HG_1G_2,C}$ (km)	6	21	12	30	19	41
$d_{\mathrm{min},HG_1G_2,S}$ (km)	5	14	9	22	14	31
$d_{\mathrm{min},HG_1G_2,M}$ (km)	3	10	6	15	10	21
$d_{\mathrm{min},HG_1G_2,E}$ (km)	2	6	4	9	7	13

Table 6.4: Same as Table 6.3 in the case of Jupiter trojans which consist mostly of D-type asteroids.

d_{AS} (AU)	5.20 ($\alpha = 0°$)	5.20 ($\alpha = 11°$)
d_{max} (km)	331	412
$d_{\mathrm{min},HG,D}$ (km)	43	74
$d_{\mathrm{min},HG_1G_2,D}$ (km)	43	67

It is nevertheless necessary to determine whether such asteroids actually exist within this parameter space, and how numerous they could be. As shown in Figure 6.5, the number of main-belt asteroids highly increases for smaller diameters. Considering an intermediate case, where all the asteroids would be located in the middle of the main belt and, using the distribution between the three main asteroid classes, around 1800 C-type asteroids, 1300 S-type asteroids and 300 M type asteroids should be within the acceptable diameter range if they are observed near opposition. These numbers are however very variable depending on the asteroid location in the solar system. Indeed, much smaller asteroids could be used as "guide star" if they are closer to the Sun and they are much more numerous than bigger asteroids. It would therefore be reasonable to conclude that

a few thousand asteroids could be used as "guide star" for observations performed when they are near opposition.

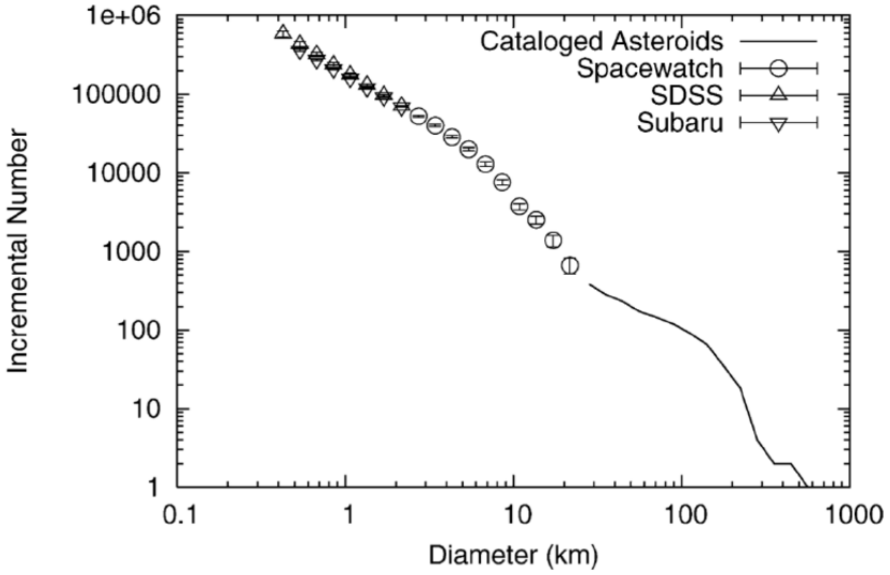

Figure 6.5: Size distribution of asteroids, with the cumulative number larger than a given diameter plotted against diameter (km). Many different determinations of this relationship are shown, each drawing data from different sources. Note that these values encompass all asteroid types [34].

The fact that the asteroids have to be near opposition is primordial. Indeed, for a distance of 2.65 AU, if the phase angle is equal to 22°, only around 230 C-type asteroids, 80 S-type and 130 M-type would be bright enough for the AO system.

Note also that if a star brighter than magnitude 12 is required for the AO system, for a distance of 2.65 AU and $\alpha = 0°$, approximately 190 C-type asteroids, 70 S-type and 120 M-type asteroid would be bright enough so that only a few hundred main-belt asteroids could be used as "guide stars".

Additionally, the fact that smaller asteroids could be used if they are in the inner part of the main-belt is of particular interest since, if an off-axis star is required for the AO system, the observation period of these asteroids was greatly limited by the higher apparent velocity in the inner part of the main-belt than in the outer part. Using these small asteroids as "guide star", there will then be no limit to the observation of these objects, except the visibility from the observatory and potentially, the phase angle.

Concerning Jupiter trojans, the number of asteroids bigger than 1 km is approximately one order of magnitude smaller than in the main-belt. Combined with a low albedo and with the fact that at such distance from the Sun, the asteroid must be much larger to be of sufficient magnitude, there will thus be only a few asteroids bright enough for the AO system. However, the fact that only a few Jupiter trojans could be used as guide "star" is less problematic because, at such a distance from the Sun, the apparent velocity of objects is slower, thus enabling longer observation windows with an off-axis guide star.

6.3 Trans-Neptunian objects

For TNOs, considering a similar brightness increase between the V-band and the K-band than for the main-belt asteroids, it appeared that they are not sufficiently bright to be used as guide star. Indeed, Makemake, the second brightest TNO after Pluto, has an apparent magnitude in V-band of 17 at opposition according to JPL ephemerides [4] and the brightness increase between the V-band and the K-band enables an average gain in brightness of 2.5 magnitudes. Therefore, it is unlikely that such objects will be brighter than magnitude 14 in K-band.

Pluto however has a magnitude of 14.5 in V-band at opposition [4] which indicates that it could have a sufficient magnitude in K-band. Several spectroscopic measurements covering various wavelengths across the K-band have already been performed and indicate an apparent magnitude around 13 in this band [35]. Concerning Pluto's angular diameter, because of its highly eccentric orbit, it will greatly vary depending on the object position on its orbit with, assuming a Sun-Earth distance of 1 AU and $\alpha = 0°$, a maximum of around 0.114" at perihelion and a minimum of approximately 0.067" at aphelion [36, 37]. Though its maximum diameter is slightly larger than the maximum value admissible for the AO system, the object could still be used as "guide star" during most of its orbit. Besides, Pluto's orbital period is very long (around 250 years) so that the angular diameter will vary slowly over the years. Since its angular diameter is around 0.088" between 2030 and 2036, Pluto could thus be used as "guide star" during several years.

CONCLUSION AND PERSPECTIVES

This thesis aimed to determine the possibilities of observations of solar system objects with the METIS instrument of the upcoming ELT. Because of the large collecting area of this telescope, adaptive optics must be used to counteract the image degradation due to atmospheric effects. This however puts stringent constraints on the possibility of observing non sidereal objects.

For the METIS AO system to work properly, a star brighter than magnitude 12 must be located within maximum 13" from the science target. These constraints could nevertheless be relaxed up to star brighter than 14 and located up to 18" to the object but at the expanse of reduced performance of the correction provided by the AO system and, in the case of the separation between the guide star and the target, more constraints on the operation of the instrument.

The guide star must also remain within 13" or 18" from the target during a sufficiently long time to enable a proper observation of the target, typically, at least 30 min. Additionally, the Sun elevation must also be below -18° and the target elevation above 30° to ensure optimal observing conditions.

Moreover, for some targets, additional constraints have been identified: the separation between a moon and its parent planet must be larger than 13.5" to ensure that the planet will always be outside METIS field of view during all the observation whereas for Jupiter's aurorae, observations in aurora zones are only interesting between specific longitude in the Jupiter System III coordinate system. Finally, for comets, a heliocentric distance smaller than 1.5 AU will ensure that the comet is sufficiently active.

All these constraints have been taken into consideration in order to develop a tool enabling to determine the number of possible observation windows and their duration for observations of solar system objects. This observability assessment tool is available in [20]. It mainly consists in two functions: a first one that returns the times for which there are stars sufficiently close to the object and a second one that determines if these times form sufficiently long windows. Additionally, a function enabling a graphical representation of the windows has also been created. These functions were then used on several targets representative of the variety of solar system objects: planets, asteroids, trans-Neptunian

objects, comets, moons and Jupiter's aurorae, providing meaningful results regarding their observation possibilities.

It first appeared that the minimum target elevation and the maximum Sun elevation required does not enable the observation of some target such as Mercury, Venus or C/2024 E1. In the case of Venus and C/2024 E1 decreasing the minimum target elevation would enable to find some windows of at least 30 min whereas for Mercury, the planet is too fast for a star to remain in a 18" region around it for a sufficiently large amount of time. Mars also has a fast apparent motion but is sometimes sufficiently slow to have a few windows of 30 min. However, none of these windows enables the entire target to be within 18" from the guide star for at least 30 min. Nevertheless, these observations correspond to times where the distance between Mars and the Earth is close to its maximum so that the angular radius of Mars is sufficiently small for the planet to be completely within the imager's field of view.

The number of windows mainly depends on the time spent by the target at a sufficiently high elevation. For the slowest targets such as Pluto or C/2014 UN271, the region of the sky in which the objects are located also influences the number of windows. Indeed, if they are located in a region of the sky where there is not a lot of stars, the number of observation windows will be very low for a long time as the target will not rapidly escape this region.

It has also been shown that several factors constraint the duration of observation windows. Targets of apparent motion larger than 10"/h such as main-belt asteroids can only lead to observation windows shorter than 2 h. This can be problematic, especially for inner main-belt asteroids for which all the observation windows are shorter than 1 h. On the other hand, slower targets can enable observations of several hours. For such slow targets, observation window durations are indeed mainly constrained by the elevation of the target and of the Sun. Additional constraints such as a minimum distance between the target and its parent planet or a specific orientation of the target also influence the length of the windows.

For comets such as 67P, the number of windows and their duration increases sharply with the heliocentric distance. This is an issue because comets are most interesting to observe when they are active, which generally happens at distances less than 1.5 AU from the Sun. However, it has been shown that at such a distance, there is no suitable observation window because of the high velocity of the targets.

For many targets, a guide star with a minimum magnitude of 12 already enables on average at least 10 observation windows per year with a guide star located within 18" from the entire target. Lower magnitude stars would however be useful to significantly increase the number of windows for objects such as Pluto or C/2014 UN271, which will remain for a long time in sparse regions of the sky, as well as for Vesta, which has a fast apparent motion.

Concerning the maximum separation between the guide star and the target, it appeared that the default distance of maximum 13" will be enough to have a large number of windows enabling to observe entirely several targets, but this number is much lower

for Uranus, Pluto, Hygiea, Vesta and C/2014 UN271. For Pluto and C/2014 UN271, this is once again explained by the slow motion of these targets in low stellar density regions whereas for Uranus, the larger angular size of this planet also reduces the region in which stars can be located if the entire planet must be within 13". For Hygiea and Vesta, the fast apparent motion of main-belt asteroids is responsible for the low number of windows in which the target is within 13" from a guide star for at least 30 min. Offsetting the science channel by 5" will thus enable to increase the observation possibilities of those targets.

As it has been shown that observation windows can be pretty rare for main-belt asteroid and TNOs as well as very short in the case of main-belt asteroids, the possibility of using these objects as "guide star" has been studied. This study has highlighted that between a few hundred to a few thousand main-belt asteroids could be used as guide object in the AO system depending on the considered required brightness. However, this number remains a rough approximation since asteroid apparent magnitude is strongly dependent on their distance to the Sun, their diameter and their albedo. Additionally, because of this dependence on the distance with respect to the Sun, an asteroid can be smaller and still observable when it is closer to Earth, which is of particular interest given the small windows obtained for observations of inner main-belt asteroids with an off-axis star. Using these asteroids as "guide star" would then enable observation windows only limited by the target visibility from the observatory and its position on its orbit.

The number of asteroids that could be used in the AO system is two orders of magnitudes smaller for Jupiter trojans so that only a few of them are sufficiently bright. However, this is less critical as these objects are located farther away and should thus enable longer observation windows.

As for the TNOs, most are too faint to be used as "guide star". Only Pluto could be sufficiently bright and has an angular size smaller than the maximum acceptable for the pyramid wavefront sensor for most of its orbit. Once again, this would enable to overcome the problem of the low number of possible observation windows and observations of Pluto would then be only limited by its visibility from the observatory.

In view of the results stated above, it would be interesting to study more deeply the possibility of guiding on science targets, especially main-belt asteroids as this would enable to have observation windows only limited by the target visibility. In particular, the results of a dedicated study on the possibility of using objects of larger angular size than the modulation radius of the METIS pyramid wavefront sensor would enable to refine the boundaries on the object size. Additionally, more data about asteroid apparent magnitudes in K-band would enable a better estimation on the number of asteroids that could be used as "guide stars". Other objects such as moons could also be studied, including the potential of using moons as guide objects for observations of giant solar system planets.

Finally, for targets for which no or only a few windows have been found, implementing the use of laser guide stars with METIS would enable to greatly increase the observation possibilities. This is especially critical for observations of comets which are scientifically

interesting when they are close to their perihelion but too fast to enable any guide star to remain within 18" from them for a sufficiently long time. Since METIS operates in the mid-infrared, a single sodium laser, among the six planned for the ELT, should already offer good adaptive optics performance for such cases.

BIBLIOGRAPHY

[1] S.P. Quanz. *METIS Science Case*. Mar. 2019. URL: https://metis.strw.leidenuniv.nl/wp-content/uploads/2021/01/E-REP-ETH-MET-1014_1-0_METIS-Science-Case.pdf.

[2] Astropy Collaboration et al. "Astropy: A community Python package for astronomy". In: *Astronomy and astrophysics* 558, A33 (Oct. 2013), A33. DOI: 10.1051/0004-6361/201322068. arXiv: 1307.6212 [astro-ph.IM].

[3] Astropy Collaboration et al. "The Astropy Project: Sustaining and Growing a Community-oriented Open-source Project and the Latest Major Release (v5.0) of the Core Package". In: *The Astrophysical Journal* 935.2, 167 (Aug. 2022), p. 167. DOI: 10.3847/1538-4357/ac7c74. arXiv: 2206.14220 [astro-ph.IM].

[4] NASA Jet Propulsion Laboratory. *HORIZONS System*. https://ssd.jpl.nasa.gov/horizons. Accessed: 2025-05-31. 2025.

[5] J.M. Beckers. "Adaptive Optics for Astronomy: Principles, Performance, and Applications". In: *Annual Review of Astronomy and Astrophysics* 31 (Jan. 1993), pp. 13–62. DOI: 10.1146/annurev.aa.31.090193.000305.

[6] R. Davies and M. Kasper. "Adaptive Optics for Astronomy". In: *Annual Review of Astronomy and Astrophysics* 50 (Sept. 2012), pp. 305–351. DOI: 10.1146/annurev-astro-081811-125447. arXiv: 1201.5741.

[7] Pa. Hickson. "Atmospheric and adaptive optics". In: *The Astronomy and Astrophysics Review* 22, 76 (Nov. 2014), p. 76. DOI: 10.1007/s00159-014-0076-9.

[8] O. Absil and G. Orban de Xivry. *Lectures notes of the Adaptive optics course*. 2025.

[9] Wikepedia. *Extremely Large Telescope*. 2025. URL: https://en.wikipedia.org/wiki/Fried_parameter (visited on 06/03/2025).

[10] ESO. *THE EXTREMELY LARGE TELESCOPE*. 2025. URL: https://elt.eso.org/ (visited on 04/23/2025).

[11] *ESO - E-ELT Optical Design*. URL: https://www.eso.org/sci/facilities/eelt/telescope/design/ (visited on 04/14/2025).

[12] Wikepedia. *Extremely Large Telescope*. 2025. URL: https://en.wikipedia.org/wiki/Extremely_Large_Telescope (visited on 04/23/2025).

[13] B. Brandl et al. "METIS: The Mid-infrared ELT Imager and Spectrograph". In: *The Messenger* 182 (Mar. 2021), pp. 22–26. DOI: 10.18727/0722-6691/5218. arXiv: 2103.11208 [astro-ph.IM].

[14] B. Brandl et al. "Status update on the development of METIS, the mid-infrared ELT imager and spectrograph". In: *Ground-based and Airborne Instrumentation for Astronomy IX*. Ed. by Christopher J. Evans, Julia J. Bryant, and Kentaro Motohara. Vol. 12184. Society of Photo-Optical Instrumentation Engineers (SPIE) Conference Series. Aug. 2022, 1218421, p. 1218421. DOI: 10.1117/12.2628331.

[15] M. Feldt et al. "High strehl and high contrast for the ELT instrument METIS". In: *Experimental Astronomy* 58.3 (Nov. 2024), p. 20. ISSN: 1572-9508. DOI: 10.1007/s10686-024-09968-2.

[16] M. Feldt. *Private communication*. 2025.

[17] G. H. Kaplan. "The IAU resolutions on astronomical reference systems, time scales, and earth rotation models : explanation and implementation". In: *U.S. Naval Observatory Circulars* 179 (Jan. 2005). DOI: 10.48550/arXiv.astro-ph/0602086. arXiv: astro-ph/0602086 [astro-ph].

[18] Tfr000. *Diagram of a star's right ascension and declination as seen from outside the celestial sphere. Depicted are the star, the Earth, lines of RA and dec, the vernal equinox, the ecliptic, the celestial equator, and the celestial poles.* June 2012. URL: https://commons.wikimedia.org/wiki/File:Ra_and_dec_on_celestial_sphere.png (visited on 05/01/2025).

[19] F. Bagenal and R.J. Wilson. *Jupiter Coordinate Systems*. Accessed: 2025-04-12. Laboratory for Atmospheric and Space Physics, University of Colorado Boulder. Aug. 2016. URL: https://lasp.colorado.edu/mop/files/2015/02/CoOrd_systems12.pdf.

[20] A. Martin. *METIS_solar*. 2025. URL: https://github.com/vortex-exoplanet/METIS_solar.git.

[21] R. van Boekel. *Observing non-sidereal objects with METIS*. May 2021.

[22] M. F. Skrutskie et al. "The Two Micron All Sky Survey (2MASS)". In: *The Astrophysical Journal* 131.2 (Feb. 2006), pp. 1163–1183. DOI: 10.1086/498708. URL: https://vizier.cds.unistra.fr/viz-bin/VizieR?-source=II/246.

[23] F. Ochsenbein, P. Bauer, and J. Marcout. "The VizieR database of astronomical catalogs". In: *Astronomy and Astrophysics Supplement Series* 143 (2000), pp. 23–32. DOI: 10.1051/aas:2000332. URL: https://doi.org/10.1051/aas:2000332.

[24] National weather service. *Twilight Types*. 2025. URL: https://www.weather.gov/lmk/twilight-types#:~:text=Astronomical%20Twilight%3A&text=Under%20astronomical%20twilight%2C%20the%20horizon,18%20degrees%20below%20the%20horizon. (visited on 11/10/2024).

[25] A. Ginsburg, T. Robitaille, et al. *Astroquery: An Astronomical Web-querying Package in Python*. Version 0.4.4. 2019. DOI: 10.5281/zenodo.2533376. URL: https://astroquery.readthedocs.io/.

[26] P.H. Bernardinelli et al. "C/2014 UN_{271} (Bernardinelli-Bernstein): The Nearly Spherical Cow of Comets". In: *The Astrophysical Journal* 921.2, L37 (Nov. 2021), p. L37. DOI: 10.3847/2041-8213/ac32d3. arXiv: 2109.09852 [astro-ph.EP].

[27] J. T. Clarke et al. "Jupiter's aurora". In: *Jupiter. The Planet, Satellites and Magnetosphere*. Ed. by Fran Bagenal, Timothy E. Dowling, and William B. McKinnon. Vol. 1. 2004, pp. 639–670.

[28] C.-I Lagerkvist and I. Williams. "Physical studies of asteroids. XV - Determination of slope parameters and absolute magnitudes for 51 asteroids". In: *Astronomy and Astrophysics Supplement Series* 68 (Feb. 1987), pp. 295–315.

[29] R. Dymock. "The H and G magnitude system for asteroids". In: *Journal of the British Astronomical Association* 117 (Dec. 2007), pp. 342–343.

[30] V. G. Shevchenko et al. "Asteroid observations at low phase angles. IV. Average parameters for the new H, G_1, G_2 magnitude system". In: *Planetary and Space Science* 123 (Apr. 2016), pp. 101–116. DOI: 10.1016/j.pss.2015.11.007.

[31] Alan W. Harris and Alan W. Harris. "On the Revision of Radiometric Albedos and Diameters of Asteroids". In: *Icarus* 126.2 (Apr. 1997), pp. 450–454. DOI: 10.1006/icar.1996.5664.

[32] T. Mueller. *Private communication*. 2025.

[33] E. Jehin. *Private communication*. 2025.

[34] K. Walsh, Patrick Michel, and Derek Richardson. "Collisional and Rotational Disruption of Asteroids". In: *Journal of Computational and Theoretical Nanoscience* 4 (June 2009). DOI: 10.1166/asl.2011.1206.

[35] T.L Roush et al. "Near-Infrared Spectral Geometric Albedos of Charon and Pluto: Constraints on Charon's Surface Composition". In: *Icarus* 119.1 (1996), pp. 214–218. ISSN: 0019-1035. DOI: https://doi.org/10.1006/icar.1996.0014. URL: https://www.sciencedirect.com/science/article/pii/S0019103596900147.

[36] Jet Propulsion Laboratory. *JPL Small-Body Database Lookup*. 2025. URL: https://ssd.jpl.nasa.gov/tools/sbdb_lookup.html (visited on 05/31/2025).

[37] Wikipedia. *Pluto*. 2025. URL: https://en.wikipedia.org/wiki/Pluto (visited on 05/31/2025).